

DISSOLUTION-INDUCED SURFACE MODIFICATIONS AND PERMEABILITY
CHANGES ASSOCIATED WITH FLUID FLOW THROUGH AN ABRADED
SAW-CUT IN SINGLE CRYSTAL QUARTZ

A Thesis

by

JAMES ALBERT BOWMAN, JR.

Submitted to the Office of Graduate Studies of
Texas A&M University
in partial fulfillment of the requirements for the degree of

MASTER OF SCIENCE

May 1992

Major Subject: **Geology**

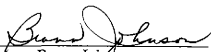
DISSOLUTION-INDUCED SURFACE MODIFICATIONS AND PERMEABILITY
CHANGES ASSOCIATED WITH FLUID FLOW THROUGH AN ABRADED
SAW-CUT IN SINGLE CRYSTAL QUARTZ

A Thesis


by

JAMES ALBERT BOWMAN, JR.

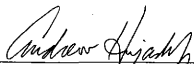
Approved as to style and content by:



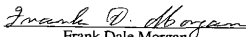
Brann Johnson
(Co-Chairman of Committee)



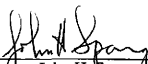
Thomas T. Tieh
(Co-Chairman of Committee)



Andrew Hajash, Jr.
(Member)



Frank Dale Morgan
(Member)



John H. Spang
(Head of Department)

May 1992

ABSTRACT

Dissolution-Induced Surface Modifications and Permeability Changes
Associated with Fluid Flow Through an Abraded Saw-Cut
in Single Crystal Quartz. (May 1992)

James Albert Bowman, Jr., B.S., West Georgia College

Co-Chairs of Advisory Committee: Dr. Brann Johnson
Dr. Thomas T. Tieh

The objectives of this research were: (1) using a through-flow system, measure temporal variations of fracture permeability induced by dissolution reactions in an artificial fracture in a quartz crystal subjected to an elevated temperature and effective-pressure state; (2) characterize modifications of the fracture surface induced by dissolution and determine the evolution of the surface texture as a function of increasing dissolution; and (3) correlate the permeability variations with observed dissolution modifications of the fracture surface.

The permeability of an abraded saw-cut oriented normal to the c-axis of a quartz crystal changed systematically with continuous flow of a dilute aqueous sodium carbonate solution under conditions of constant volume flow rate (2 ml/hr), temperature (155°C), and effective pressure (10 MPa). Fracture permeability slowly decreased during the initial 25 hours and then increased at an escalating rate. After 60 hours of flow, the permeability was 40 times greater than the initial value. Dissolution widening of the fracture aperture was not uniformly distributed but was localized along several axial dissolution channels. Formation of the dissolution channels reflects a positive-feedback process between flow rate, permeability and dissolution rate. A separate experiment showed that the rate of permeability increase was greater for larger flow rates.

Abrasion-induced microcracks exerted the dominant control on dissolution modification of the surface texture with increasing dissolution. Five types of dissolution-induced surface elements of distinct morphology developed and exhibited a systematic spatial distribution on a transverse section of a dissolution channel. Each dissolution surface element represents a different stage in the evolution of a dissolving microcrack. Depending upon the initial depth of penetration of the crack, dissolution-modification of a crack follows one of two evolution scenarios. Cracks penetrating deeper than about 10 μm acquire dissolution forms reflecting a crystallographic control on dissolution. Dissolving cracks widen by a combination of parallel retreat and "laying back" of the walls of the dissolution element. Parallel retreat following a phase of "laying back" occurs when

stage of a dissolving crack was a flat-floored polygonal basin, which widens and deepens by a parallel retreat of the walls and floor. The stage to which a crack has evolved after a specific amount of dissolution is directly related to its initial depth of penetration. Shallower cracks attain more advanced stages of dissolution modification than deeper cracks, for the same net amount of dissolution.

The evolution of the overall surface texture reflects evolution of individual dissolving cracks and their "interaction" with neighboring elements. A distribution of depths of penetration of the initial cracks results in a population of dissolution surface elements with morphologies corresponding to differing stages of the evolution sequence of a dissolving crack. As individual elements widen their areal extent increases and eventually overlaps that of neighboring elements. The amount of dissolution required for onset of element interaction is related to the spacing between the initial microcracks. The relative depths of neighboring elements determines the subsequent events after onset of overlap. Widening of the deeper elements, which are derived from the deeper penetrating cracks, ultimately annihilates the shallower neighboring elements. Consequently, with increasing dissolution, the surface is comprised of progressively fewer, but larger, dissolution elements derived from the deeper penetrating cracks of the initial microcrack population.

DEDICATED TO
MY PARENTS

ACKNOWLEDGEMENTS

My highest praise is extended to my advisor, Dr. Brann Johnson, who developed the permeability system for this research and provided an organization for presenting our data. Without his extraordinary help and commitment during the final stages of this research, this thesis would not have been possible. I am very grateful to him for helping me to learn and become a better scientist. My committee co-chairman, Dr. Tom Tieh, was very helpful by providing encouragement and technical advice on experimental methods and quartz crystallography. I also thank my other committee members, Drs. Andy Hajash and Dale Morgan, for their insights into fluid/rock interactions given during seminars and lectures as well as their editorial comments on the thesis. This research was satisfying due to the involvement of my father who, during a trip to Texas, helped me work through problems regarding the permeability system and offered advice on the data presentation. Randy Scott of the Electron Microscopy Center at Texas A&M University offered valuable assistance preparing samples for the SEM imaging and photography. I am grateful also to Bill McFall of Brown Environmental, Inc. and Chuck Gorman of the South Carolina Department of Health and Environmental Control for granting me academic leave from work during the thesis preparation. I especially acknowledge two individuals, Judy Canova and Mair DePratter, who worked diligently to help me in the final stage of preparing photographs and figures for the thesis manuscript.

Partial financial support for this research was provided by a grant from the Structural Geology Research Group of the Amoco Production Company, Tulsa, Oklahoma.

TABLE OF CONTENTS

	Page
INTRODUCTION	1
PREVIOUS WORK	3
QUARTZ.....	3
Crystallography and Crystal Forms	3
Cleavage.....	3
DISSOLUTION KINETICS OF QUARTZ; CRYSTALLOGRAPHIC CONTROL	5
DISSOLUTION SURFACE FEATURES	7
General Aspects	7
Etch Pits	9
Microcracks and Holes	10
EVOLUTION OF DISSOLUTION SURFACE TEXTURES	13
METHODS AND MATERIALS	16
SAMPLE ORIENTATION AND PREPARATION.....	16
SAMPLE ASSEMBLY.....	17
EXPERIMENTAL SYSTEM.....	17
EXPERIMENTAL PROCEDURE.....	20
PERMEABILITY MEASUREMENTS AND CALCULATIONS.....	20
CHARACTERIZATION OF DISSOLUTION-INDUCED SURFACE FEATURES.....	21
PERMEABILITY VARIATIONS WITH TIME.....	23
EXPERIMENT Q1.....	23
Part I.....	23
Part II.....	24
EXPERIMENT Q2.....	27
DISSOLUTION MODIFICATION OF ABRADED SURFACES	29
MACROSCOPIC CHARACTERISTICS	29
MICROSCOPIC CHARACTERISTICS OF REACTED SURFACE	32
Introduction	32
Secondary Mineral Formation	32
SEM Transect.....	34
Interval of Indiscernible Dissolution	38
Dissolution Interval I.....	41
Dissolution Interval II.....	44
Dissolution Interval III.....	48
Etched Cracks and Polygonal Widened Cracks.....	48
Cusplate and V-Shaped Notches	59
Relation Between Polygonal Widened Cracks and V-Shaped Notches.....	61
Relation Between Cusplate Notches and V-Shaped Notches	61
Dissolution Interval IV.....	61

TABLE OF CONTENTS (Continued)

	Page
Conceptual Evolution Scenarios for Dissolution Modification of Cracks	66
Scenario I	67
Scenario II	67
Evolution of the Overall Surface Texture with Increasing Extent of Dissolution	69
Comparison Of Surface Textures of A Reacted Abraded M-Plane And Basal Plane	74
Relationship Between Permeability Changes and Dissolution-Induced Surface Modifications	76
MAJOR OBSERVATIONS AND CONCLUSIONS	79
TEMPORAL VARIATIONS OF FRACTURE PERMEABILITY AND THE RELATION TO DISSOLUTION EFFECTS	79
DISSOLUTION MODIFICATION OF AN ABRADED SURFACE	80
REFERENCES CITED	82
VITA	84

LIST OF FIGURES

Figure		Page
1	Crystallographic axes and common crystal forms of quartz	4
2	Shape changes of a quartz sphere extensively dissolved in HF acid.	6
3	Relative growth rates of quartz in a Na ₂ CO ₃ solution as a function of crystallographic direction.....	8
4	Geometry and crystallographic orientation of negative crystal developed on m-plane of quartz dissolved in a weak basic solution.....	11
5	Two contrasting evolution scenarios depicting the role of crystallographic control on dissolution modification of a surface microcrack.....	12
6	SEM photographs showing progressive modification of an initially flat, polished surface of Sioux Quartzite subjected to increasing amounts of dissolution.	14
7	Sample assembly for experiments Q1 and Q2.....	18
8	Schematic diagram of the flow-through experiment system.....	19
9	Variation of permeability as a function of net flow time and changes of effective pressure during part I of experiment Q1.....	25
10	Permeability variation as function of net flow time during part II of experiment Q1.....	26
11	Variation of permeability as a function of net flow time under constant flow rate, temperature and effective pressure.	28
12	Dissolution channels developed on abraded saw-cut surface of samples Q1 and Q2.....	30
13	Surface profile across half of the major dissolution channel on sample Q2.....	31
14	Analcite crystals (a) on reacted surface of Q2.....	33
15	SEM photographs of selected locations along transect showing progressive dissolution modifications of the surface.	35
16	Spatial relations of surface elements on the SEM transect on Q2.....	37

LIST OF FIGURES (Continued)

Figure	Page
17 SEM stereo photographs of an area in the interval of indiscernible dissolution.	39
18 SEM stereo photographs of microtopography of abraded quartz surface in an area of indiscernible dissolution.....	40
19 Frequency distribution of length of abrasion cracks in Area A, which is in the interval of indiscernible dissolution.....	42
20 SEM stereo photographs of a representative area on dissolution interval I.....	43
21 Cross section profiles of cusped and v-shaped notches.	45
22 SEM stereo photographs of representative areas in dissolution interval II.....	46
23 Frequency distribution of the length of etched cracks and cusped and v-shaped notches on Area B in dissolution interval II.....	47
24 SEM stereo photographs of representative areas of the initial stage of dissolution interval III.....	49
25 SEM stereo photographs of representative areas of the intermediate stage of dissolution interval III.....	50
26 Cross sectional profile of a polygonal widened crack.....	51
27 SEM stereo photographs of representative area of the advanced stage of dissolution interval III.....	52
28 SEM photographs comparing surface modifications along dissolution interval III.....	53
29 SEM stereo photographs of representative areas of the advanced stage of dissolution interval III.....	55
30 Frequency distributions of the length and aperture of etched and polygonal widened cracks from Areas C and D on dissolution interval III.....	56
31 Scatter plot of length versus aperture of etched and polygonal widened cracks in Area D in the advanced stage of dissolution interval III.....	58
32 Rose diagrams of the orientation of cracks, etched cracks and polygonal widened cracks in four areas along the SEM transect.....	60

LIST OF FIGURES (Continued)

Figure		Page
33	Frequency distributions of the length of cusped and v-shaped notches in Areas C and D on dissolution interval III.	62
34	SEM stereo photographs of areas in the initial stage of dissolution interval IV.	63
35	SEM stereo photographs of representative areas in the advanced stage of dissolution interval IV.	64
36	Conceptual models of the dissolution-induced evolution of a surface microcrack.	68
37	Conceptual model for the dissolution-induced evolution of the surface of quartz with an initial population of microcracks.	71
38	SEM stereo photographs of two areas along the transect on the upstream end of sample Q2.	75

INTRODUCTION

Macrofractures are an important type of secondary porosity and control the permeability of tight sedimentary and crystalline rock masses. At a given stress state, fracture permeability depends on the details of geometry and spatial relations of the fracture pore space, which is controlled by the surface texture, roughness, and degree of mating of the contacting fracture surfaces.

Experiments (Johnson, 1983) have shown that dissolution reactions can dramatically modify the texture and roughness of a non-load-bearing fracture surface. These changes of surface texture changes are inferred to significantly affect fracture permeability. Unfortunately, there have been few measurements of fracture permeability with time under conditions in which dissolution reactions occur. Consequently, there are limited data to assist development of models that describe permeability variations associated with dissolution.

Within the above context, this research has the following objectives: (1) using a flow-through system, measure temporal variations of fracture permeability associated with dissolution reactions occurring in an artificial fracture in a quartz crystal subjected to an elevated temperature and effective pressure state; (2) characterize modifications of the fracture surface texture associated with the dissolution reactions and determine the progressive changes a surface evolves through as a consequence of dissolution reactions; and (3) attempt to correlate the measured variations of fracture permeability with the observed dissolution-induced modifications of the fracture surface.

A quartz/ aqueous sodium carbonate geochemical system was selected for the flow-through experiments. Quartz was selected because of a reasonable good geochemical data base and the fact that quartz/aqueous solution systems are relatively simple, yet of importance in many geologic settings. A sodium carbonate solution was selected in order to enhance the solubility of quartz and facilitate significant permeability changes over a reasonable time period. This geochemical system also was selected with the intent of avoiding complicating effects associated with formation of secondary products, because such by-products were not anticipated.

This research was the first to utilize a newly constructed permeability system capable of controlled, very low flow rates at a constant back pressure using corrosive fluids at an elevated temperature and pressure while the sample is subjected to a hydrostatic

confining pressure. Early experiments used polycrystalline Sioux Quartzite, but single crystals of quartz were used subsequently. As a consequence of numerous experimental problems and "debugging" of the system and experimental techniques the results of the early experiments are of limited use, hence only the results of two successful single crystal quartz experiments are reported in this thesis. The overall results from these two experiments are very similar.

Fracture permeability varied in a systematic fashion with increasing duration of fluid flow. One experiment investigated the role of flow rate and changes of effective pressure on temporal variations of permeability, whereas the other kept flow rate and effective pressure constant. After an initial stage in which permeability either remained constant or slowly decreased, depending upon the specific experiment, the permeability progressively increased at an ever escalating rate with increasing flow duration. Variation of flow rate discernibly affected rates of permeability increase.

The permeability increase correlated with development of discrete dissolution-induced flow channels on the surface of the macrofracture. Dissolution was greatest along the center of the channels and decreased progressively toward the margins of the channels. This systematic spatial variation of dissolution modification of an initial statistically homogeneous surface permitted the characterization of the evolution of dissolution-induced changes of the surface texture, which was dominated by the dissolution modification of an initial population of microcracks in the surface of the macrofracture. By knowing both the evolution of forms of dissolution elements derived from an initial microcrack and the role of "interference" of evolving neighboring dissolution elements, it was possible to understand the observed evolution of the overall surface texture of the macrofracture. Understanding the evolution of the macrofracture surface texture with increasing dissolution, in turn, provided insight into the temporal variation of fracture permeability associated with dissolution reactions.

PREVIOUS WORK

QUARTZ

Crystallography and Crystal Forms

Quartz (alpha polymorph) is a member of the trigonal trapezohedral symmetry class (32). Using the convention of Bravais, the crystallographic axes consist of three co-planar a-axes with positive ends separated by 120° , and a c-axis orthogonal to the plane of the a-axes (Figure 1). The c-axis represents an axis of three-fold rotation (120°), and each a-axis is an axis of two-fold rotation (180°).

Quartz exhibits a large number of crystal growth forms, where each form is a set of crystal faces that have the same relation to the symmetry elements of the crystal. Frondel (1962) records 112 well established forms and mentions that several hundred additional very rare or questionable forms have been reported. The most common forms occurring on quartz crystals are: hexagonal prism (m-plane) $\{10\bar{1}0\}$; major and minor rhombohedra (r-plane) $\{10\bar{1}1\}$ and (z-plane) $\{01\bar{1}1\}$, respectively; trigonal dipyrmaid (s-plane) $\{11\bar{2}1\}$; and trigonal trapezohedron(x-plane) $\{51\bar{6}1\}$.

The wide diversity of observed growth forms is important relative to the nature of crystallographic-controlled dissolution of quartz, because growth forms are usually correlated to local minima in growth rates, which, in turn, often are inferred to correspond to directions of dissolution rate minima.

In addition to the growth forms with rational indices, quartz also exhibits vicinal surfaces, which are planar or gently curvilinear surfaces that mimic crystal forms but have irrational indices (Fron del, 1962). Vicinal surfaces can occur as a result of growth or dissolution.

Cleavage

Quartz exhibits a weak, but discernible cleavage on the following seven crystal forms: r $\{10\bar{1}1\}$, z $\{01\bar{1}1\}$, m $\{10\bar{1}0\}$, c $\{0001\}$, a $\{11\bar{2}0\}$, s $\{11\bar{2}1\}$ and x $\{51\bar{6}1\}$ (Fron del, 1962). Cleavage is best developed parallel to the r, z, and m planes. These cleavage directions discernibly affect crack propagation paths in quartz as seen most notably during thermal-shock fracture and the development of contact-induced cone and sliding abrasion cracks (Fron del, 1962).

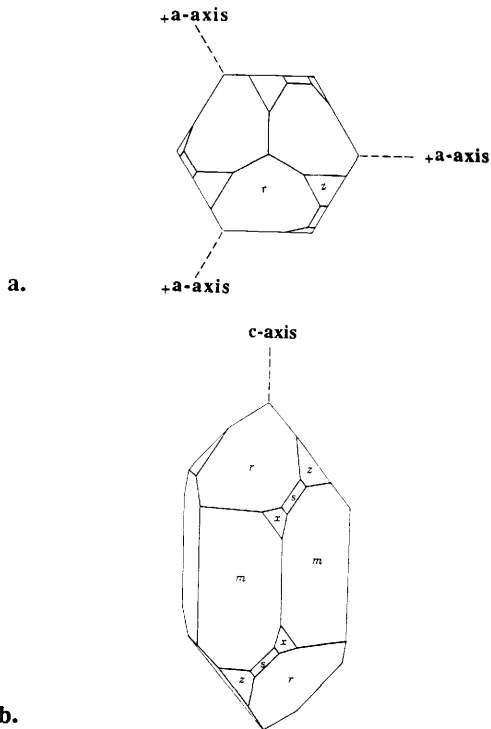


Figure 1. Crystallographic axes and common crystal forms of quartz. a) View parallel to c-axis. b) Oblique view showing common growth forms. After Frondel (1962).

DISSOLUTION KINETICS OF QUARTZ: CRYSTALLOGRAPHIC CONTROL

There have been few kinetics studies that focus on the variation of rates of quartz dissolution as a function of crystallographic direction. These limited studies show that solvent chemistry and temperature influence crystallographic control of dissolution of quartz. For example, HF acid solutions produce differing directional dissolution rates as compared with basic solutions.

Frondel (1962) summarizes results of other researchers on the directional variation of dissolution rates of quartz in HF acid solutions. These experiments utilized either polished spheres, natural crystal faces or cut and polished oriented sections. Quartz spheres extensively dissolved in HF transform into a triangular lenticular shape (Figure 2). In HF, the rate of dissolution is maximum for the basal plane (0001) and a minimum for a-planes {11 $\bar{2}$ 0}. Extensive dissolution of selected crystal faces and crystallographically oriented, polished sections shows the rate of dissolution decreases for selected planes in the following order: {0001} >> {01 $\bar{1}$ 1} > {10 $\bar{1}$ 1} >> {10 $\bar{1}$ 0} (i.e. basal section >> z-plane > r-plane >> m-face). There is a 100-fold difference in rates between the basal section and the m-plane.

Gratz and others (1990) studied dissolution of natural and polished rhombohedral and prism planes in 10^{-4} - 10^{-1} M alkali hydroxide solutions at temperatures from 106-236°C. Measured dissolution rates vary with temperature, the OH⁻ activity and alkali species. For a fixed chemical and temperature state, the order of decreasing dissolution rate for the three crystal forms studied is z-plane > r-plane > m-plane. The rates for the z- and r-planes differ by 15%. Whereas, for the range of temperatures and OH⁻ activities used, the ratio of dissolution rates of rhombohedral to prism planes varies from 1.5 to 2.9. The contrast between the dissolution rates of rhombohedral and prism planes increases with increasing temperature and decreasing OH⁻ activity. Although they obtained rates for only three specific crystallographic directions, they estimate the minimum contrast between the fastest and slowest dissolution directions is about 5. They, however, report that Liepmann (1985) estimated the minimum contrast between fastest and slowest directions of quartz dissolution to be about 10 for a solution with a greater OH⁻ activity at a temperature of 90°C.

Many researchers consider dissolution and crystallization processes to be similar, hence one might predict the directional variations of quartz growth and dissolution to be similar in an identical chemical environment. This prediction, however, appears to be only approximately correct, as shown by a comparison of quartz growth rate data of Ballman

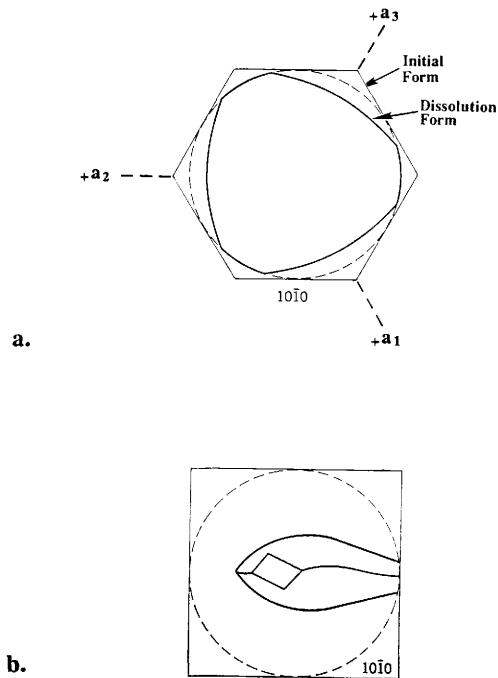


Figure 2. Shape changes of a quartz sphere extensively dissolved in HF acid. a) Initial and final profiles in a basal plane (0001). b) Initial and final profiles in a plane parallel to m -plane. Modified from Frondel (1962).

and Landise (1963) and the more limited dissolution rate data of Gratz and others (1990). For quartz grown in a Na_2CO_3 solution (a very basic solution) at 350°C, there is a significantly greater contrast in rates of growth of the rhombohedral and prism planes (Figure 3) than observed for the rates of dissolution of the corresponding planes. Part of this discrepancy may reflect a temperature effect. Nevertheless, it suggests one should be careful when making quantitative predictions of dissolution rates using growth-rate data. It is noteworthy that the sequential order according to dissolution rates measured by Gratz and others (1990) are consistent with the growth data. If this sequential order applies to other crystallographic directions, then the dissolution rate parallel to the c-axis in basic solutions should be greater than the rates for r, z and m planes but smaller than for directions somewhat oblique to the c-axis.

DISSOLUTION SURFACE FEATURES

General Aspects

Quartz dissolution is a surface reaction rate-limited process in which intracrystalline defects and free-surface irregularities play a key role (Berner, 1978). Dissolution occurs by the development and lateral migration of a series of lattice-scale steps that nucleate at either of two basic types of surface "active sites": (1) lattice distortions adjacent the surface or (2) free-surface edges or corners. Emergent dislocations and point defects represent the dominant lattice distortion features, whereas on an abraded surface, microcracks constitute a prominent source of free-surface edges and corners.

The model of Hirth and Pound (1957) predicts the speed of migrating steps, hence spacing, increases away from the site of step nucleation until achieving a steady rate at a characteristic distance, and the spacing between adjacent migrating steps increase progressively away from the site of step nucleation. With attainment of this steady-state, the spacing between steps remains constant and the local dissolution surface has a planar appearance, like a crystal facet.

The local curvature of a dissolving surface plays an important role in the evolution of the local surface morphology. Convex and concave surface features can evolve differently as shown by several simple experiments reported by Frondel (1962) and Correns (1969). Correns notes that an initially circular hole in a mineral that exhibits crystallographic controlled dissolution widens during extensive dissolution and acquires a polygonal shape with facets that correspond to growth forms. He refers to these dissolution forms as "negative crystals." In contrast, extensive dissolution of a convex

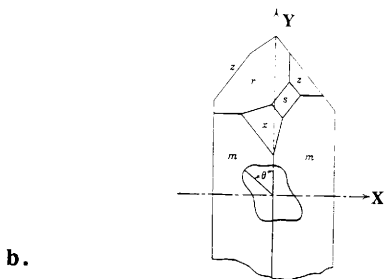
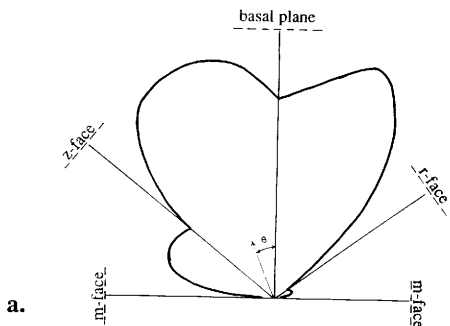


Figure 3. Relative growth rates of quartz in a Na_2CO_3 solution as a function of crystallographic direction. a) Relative growth rates as a function of radial direction in a plane parallel to the c-axis and perpendicular to a m-plane (X-Y plane). b) Orientation of X-Y plane relative to common crystal forms.

surface, such as the surface of a sphere, does not produce a faceted appearance; instead, the surface acquires a modified rounded shape that reflects the directional variations of the dissolution rates (Frondel, 1962). From this observation, one might expect a hemispherical asperity on a surface of quartz to transform into a rounded, nonspherical form with an amplitude that decreases with increasing dissolution.

In general, localized enhanced dissolution of quartz occurs primarily in association with either surface microcracks and holes or emergent dislocations. Enhanced dissolution at emergent dislocations results in surface features referred to as "etch pits." Observations of Johnson (1983) and Hicks (1985) indicate that, if microcracks are abundant, the role of dislocation etch pits on evolution of surface morphology is largely overshadowed, especially if dissolution is extensive. This is the case for the abraded quartz surfaces used in the current study. Nevertheless, there are certain aspects of etch pit development that appear to provide insight into the dissolution modification of microcracks. These pertinent aspects of etch pits are briefly summarized below.

Etch Pits

The morphology of dislocation etch pits in quartz is highly variable and depends upon the solvent chemistry, temperature, extent of dissolution and the crystallographic orientation of the dissolving macroscopic surface (cf. Frondel, 1962; Wegner and Christie, 1983). A number of solvents and etching conditions produce etch pits with morphologies that reflect crystallographic control on dissolution. This type of dissolution is typically referred to as "preferential dissolution" and produces etch pits consisting of a system of planar or curvilinear facets. Usually, the symmetry of the facets of the etch pit reflects that of quartz.

Joshi and Vagh (1968) and Hicks (1985) describe development of dislocation etch pits on rhombohedral planes of quartz; their observations are of particular interest to the present study. Dissolution of the rhombohedral plane in either H₂O or a NaOH solution produces etch pits having the form of an inverted three-sided pyramid. The sharp apex is interpreted to be centered on the penetrative dislocation line. With increasing dissolution these sharp-bottomed pits deepen and widen but not without limit. It is observed that with increasing dissolution individual sharp-bottomed etch pits change form to that of a three-sided flat-floored pit. Joshi and Vagh (1968) suggest that the sharp-bottom form reflects control of deepening by enhanced dissolution centered on the dislocation line. When the terminus of the dislocation line is reached, continued localization is not possible and the etch pit changes shape to a form that reflects other crystallographic controls on dissolution.

Microcracks and Holes

Numerous researchers have noted that dissolution highlights surface microcracks and holes on quartz surfaces. If dissolution is of a limited extent, the most prominent evidence of dissolution modification of a microcrack is the discernible increase in crack aperture. With more extensive dissolution, microcracks and holes (usually cylindrical tubules) widen further and the outline of the well-defined upper edge has a polygonal shape, which reflects crystallographic control on dissolution (cf. Johnson, 1983). With even greater dissolution, some researchers (Joshi and Vagh, 1968; Johnson, 1983; Hicks, 1985; Gratz and others, 1990) infer that cracks evolve into a broad polygonal-shaped depression often with a flat floor. Gratz and others (1990) refer to these surface elements as negative crystals because walls of the depressions correspond to crystallographic forms. On a *m*-plane, the negative crystals are rectangular in shape with the long axis parallel to the *c*-axis and facets identified as specific crystal planes (Figure 4). The long walls and floor are *m*-planes, whereas the two shorter walls are *r*- and *z*-planes. On a rhombohedral surface, negative crystals form and are triangular with all facets being rhombohedral planes. Determination of dissolution rates of *m*-, *r*-, and *z*-planes entails measuring the rate of retreat of the facets of the negative crystals as a function of time.

Although several distinct forms of dissolution-modified microcracks are indicated by previous workers, details of the evolution of their dissolution forms remain undocumented. Gross (1918), however, presents a simple model that shows how a crack evolves into a negative crystal, if conditions are favorable (Figure 5). His model entails a simple geometric construction and knowledge of a velocity surface that represents the variation of dissolution rates as a function of direction. In his model, the local maxima and minima of dissolution rates and their orientation relative to the macroscopic surface determine the idealized form of the widening crack. Development of facets of the negative crystal correlates with the slow dissolving directions. According to Gross's model, two conditions must exist concurrently in order for a crack to evolve into a negative crystal. First, dissolution must be crystallographically controlled and certain directions must exhibit local minima in the dissolution rates. Second, the dissolving macroscopic surface must be approximately perpendicular to a direction of a local minima in dissolution rates. Under these conditions, the crack widens in the fast dissolution direction sufficiently such that slow dissolution crystal facets can develop adjacent the crack tip prior to the overall macroscopic surface being lowered to depth of the crack tip. Once this critical step is achieved, subsequent dissolution entails lateral parallel retreat of the slow dissolution

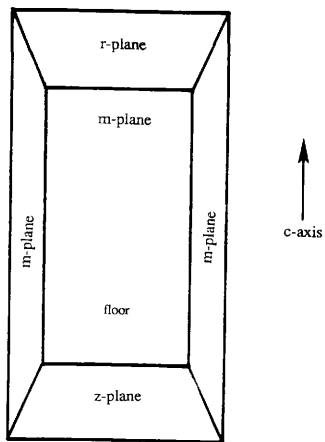


Figure 4. Geometry and crystallographic orientation of negative crystal developed on m-plane of quartz dissolved in a weak basic solution. After Gratz and others (1990).

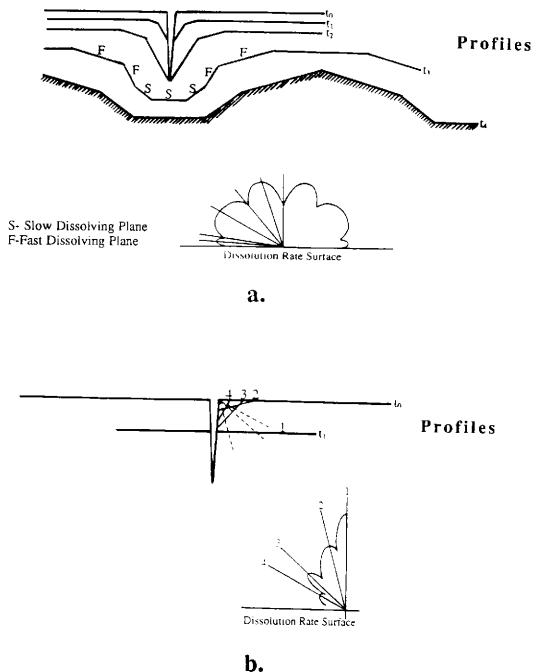


Figure 5. Two contrasting evolution scenarios depicting the role of crystallographic control on dissolution modification of a surface microcrack. Figure shows surface profiles of dissolution features at differing times. Also shown are the corresponding relative rates of dissolution as a function of radial direction in the plane of the profiles. a) Development of a negative crystal when slow dissolution direction is normal to initial surface. b) Case when crack does not evolve into negative crystal because direction of rapid dissolution is normal to initial surface. Modified from Gross (1918).

crystal facets and development of a widening, planar floor that moves downward at the same rate as the overall macroscopic surface, such that the relative depth of the negative crystal does not change with time. This evolution scenario is in contrast to the case when the direction normal to the macroscopic surface is a direction of rapid dissolution. In this case, the upper surface is lowered to the depth of the crack tip prior to sufficient widening of the crack to permit development of slow dissolution facet adjacent the crack tip.

EVOLUTION OF DISSOLUTION SURFACE TEXTURES

Johnson (1983) studied the evolution of dissolution textures for surfaces on Sioux Quartzite reacted at 200° C in distilled water and a 0.05 - 4.0 N aqueous Na_2CO_3 solution. His work utilized two markedly different starting surface textures; polished, optically flat surfaces and tensile-fracture surfaces. Microcracks, holes and tubules, and irregularities on grain boundaries and fracture surfaces are the dominant active sites for localized dissolution; effects of dislocations on dissolution surface textures were overshadowed. On the polished surfaces, abrasion-induced and natural microcracks dominate over all other active sites. The evolution of the dissolution surface texture on the tensile fracture surface differs significantly from that on the polished surface, except after extensive dissolution. The difference in the evolutions is attributed to differences in the initial microcrack populations.

The observed evolution of the polished surface texture (Figure 6) is instructive for the present study, because abrasion-induced microcracks are the prominent, if not dominant, microcracks in both cases. On the polished surfaces, the size distribution of the abrasion-induced microcracks is highly skewed toward short lengths, such that the spacing between cracks is closely correlated to crack spacing; i.e. on average, the shorter cracks are more closely spaced than the longer cracks. With increasing dissolution, the aperture of cracks progressively widened, but the spacing between neighboring cracks places an upper limit on permissible widening before interference between neighboring cracks occurs. Ultimately, as neighboring widening cracks overlap, the shallower (usually shorter) cracks are annihilated by the deeper cracks. With extensive dissolution, the surface morphology is dominated by the deeper, longer, more widely spaced cracks. The shape of these modified deeper cracks is usually polygonal in form, but typically does not possess the perfect negative-crystal form reported by Gratz and others (1990).

Gratz and others (1990) did not document the initial and intermediate phases of dissolution modification of microcracks, but the photographs they present document the subsequent stage in which negative crystals develop. Once a negative crystal forms, it

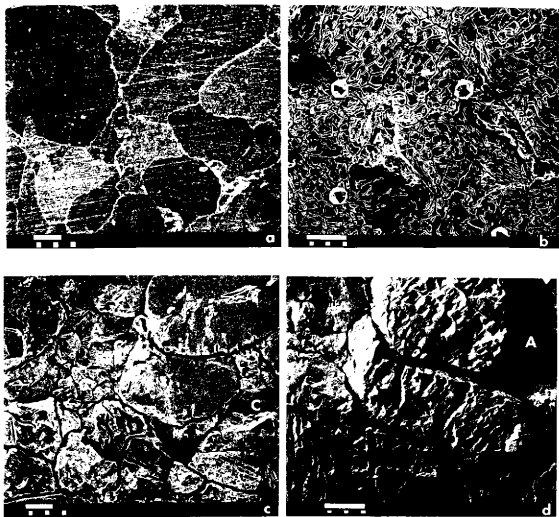


Figure 6. SEM photographs showing progressive modification of an initially flat, polished surface of Sioux Quartzite subjected to increasing amounts of dissolution. Extent of dissolution increases from (a) to (d). From Johnson (1983).

progressively widens with increasing dissolution until it overlaps neighboring negative crystals . The subsequent fate of the element and its neighbors depends upon the relative depths of the floors of the negative crystals. If a significant difference in the floor depth exists, then the shallower element is progressively annihilated by the deeper neighbors. In contrast, if their depths are comparable, both elements lose their identity and are replaced by a gently concave depression separated from its similar neighbor by a low amplitude, sharp divide.

METHODS AND MATERIALS

SAMPLE ORIENTATION AND PREPARATION

Results of two flow-through experiments are reported in this thesis. The two experiments, denoted as Q1 and Q2, used samples from two different single crystals of Brazilian quartz. The Q1 sample was cored from a broken crystal that possessed only the six prism faces; consequently, there is a 60° uncertainty of the orientation of the positive a-axes. The Q2 sample was cored from a crystal that displayed a prism face, two rhombohedral faces and a s-face. The observed difference in the outline of percussion figures on the two rhombohedral faces (Fron del, 1962) differentiated the r-face from the z-face. The position of the s-face relative to the r-and prism faces indicated the crystal had a right-handed structure. These observations permitted a unique determination of the orientation of the a-axes for the Q2 sample.

The initial stage of sample preparation entailed diamond sawing each crystal in half along a plane perpendicular to the c-axis. Each half was ground flat on a planar glass plate using 120 SiC grit (~100 μm grit diameter). Then the two halves were bonded together, and the re-assembled crystal was diamond cored perpendicular to a prism face and parallel to the abraded saw cut, which was centrally positioned and parallel to the long axis of the core. The sequence of grinding and then overcoring was utilized to prevent abrasive rounding of the saw cut adjacent outer edges of the sample, which could subsequently localize fluid flow along the edges of the abraded surface during a flow-through experiment. The ends of the cylinder were cut perpendicular to the cylinder axis (ends are parallel to a prism plane). The end surfaces were carefully ground to produce parallel ends with sharp edges to assure alignment and prevent jacket punctures. The sample halves were separated by dissolving the glue, and then the abraded surfaces cleaned ultrasonically in acetone. The last stage of sample preparation entailed a final directional abrasion of the two halves with several passes on a 120 grit quartz sandpaper. For Q1, one half was abraded parallel to the long axis and the other half was abraded perpendicular to the long axis of the sample. For Q2, both halves were abraded parallel to the long-axis of the sample. Sample halves were subjected to a final ultrasonic cleaning in acetone.

The Q1 sample was used in several unsuccessful experiments prior to the experiment reported in the thesis. Prior to the directional abrasion described above, the sample halves also were re-abraded on a glass plate with 120 grit. These deviation from the preferred preparation sequence probably resulted in some abrasional rounding of the

surface adjacent the outer edges. This rounding of the edges of the saw-cut surface appeared to localize flow along the edges of the sample during the flow-through experiments.

SAMPLE ASSEMBLY

The sample assembly (Figure 7) consisted of: (1) a 1.84 cm diameter quartz cylinder, (2) one or more Hastelloy C-276 sintered, porous discs, which served both as spacers and fluid spreaders, and (3) HC-276 endpieces with a centrally positioned, pore-fluid access hole. The Q1 sample was 3.1 cm long and the assembly utilized one porous disc upstream and two discs downstream. Q2 was 2.0 cm long and the assembly consisted of five discs upstream and one disc downstream.

The sample assembly was encapsulated by a heat-shrinkable teflon jacket. The pressure seal of the jacket with the endpieces was accomplished using hemispherical metal rings that were pressed over the 1^o tapered endpieces using an arbor press and die assembly. In order to inhibit possible flow between the jacket and sample, two wire bands were wrapped tightly around the jacketed sample near both ends.

EXPERIMENTAL SYSTEM

In general terms, the jacketed sample was hydrostatically loaded in a pressure vessel heated to a uniform elevated temperature, and pore-fluid was pumped through the sample at a controlled volumetric flow rate while the downstream pore-fluid pressure was maintained constant. The pore-fluid pressure change occurring across the sample and the volumetric flow rate were measured and recorded continuously during an experiment.

The fluid-flow system and associated permeability-measurement system were the critical subsystems with regard to these experiments (Figure 8). Controlled volumetric flow was achieved using a syringe pump upstream of the sample, while a second syringe pump downstream operated in reverse at a controlled rate in order to maintain a prescribed back pressure. All wetted parts at an elevated temperature were made of Hastelloy C-276 in order to minimize corrosion. A 55 ml in-line tubular reaction vessel was positioned upstream of the sample and served as the reservoir for the reactive Na_2CO_3 solutions. Distilled water from the upstream syringe pump displaced the reactive fluid from the vertically oriented reservoir, which was recharged after about 40 ml was displaced. The pore-fluid passed through a 2 μm filter prior to entering the pressure vessel. The pressure drop associated with flow through the sample was measured external of the vessel using a

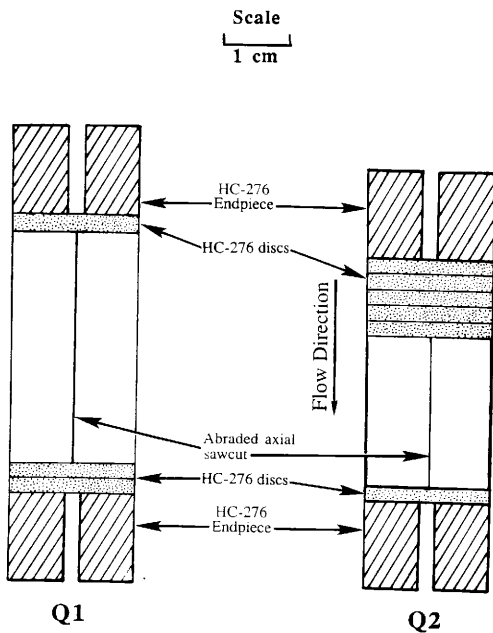


Figure 7. Sample assembly for experiments Q1 and Q2.

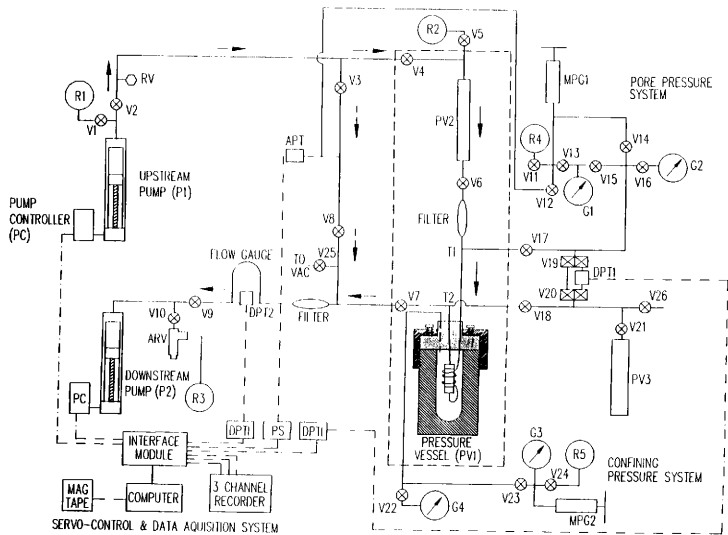


Figure 8. Schematic diagram of the flow-through experiment system.

high resolution, variable range, differential pressure transducer. Corrections for pressure losses in the intervening tubing and sintered discs were taken into account in permeability calculations. Monitoring of the volumetric flow rate was achieved using a second differential pressure transducer and measuring the pressure change across an in-line flow element of known permeability. Data from transducers are recorded in analog form on a strip chart.

Confining pressure was controlled independently from the pore-fluid pressure by means of a manually operated intensifier. The confining pressure was monitored with a visual pressure gauge. The vessel was heated externally with a series of strip heaters with power to heaters controlled manually with a powerstat. Temperature inside the vessel was measured using an internal thermocouple with the sensor tip positioned immediately adjacent the midsection of the jacketed sample.

EXPERIMENTAL PROCEDURE

An experiment entailed the following sequential steps. (1) The sample and associated pore-fluid lines were vacuum evacuation and then back filled with the working fluid. (2) The pore-fluid pressure (p_f) and the confining-fluid pressure (p_c) were increased to pre-determined values in an incremental manner so as not to exceed a prescribed effective pressure ($p_c - p_f$). (3) Fluid flow was commenced and pump rates adjusted in order to establish the desired volume flow rate and back pressure. (4) The permeability of the sample was measured at room temperature. Then pumps were shut off prior to onset of heating interval (5) The pressure vessel was slowly heated to prescribed temperature and confining and pore pressures were adjusted to maintain prescribed values. (6) Once steady-state temperature was established, flow was re-established and permeability data continuously recorded. (7) Upon conclusion of the experiment, the vessel was cooled while both the pore-fluid and confining pressures were adjusted so as not to exceed the effective pressure existing at the termination of flow. (8) Upon attaining room temperature, pore and confining pressure were reduced incrementally to zero in a fashion so as to no exceed the prior maximum effective pressure.

PERMEABILITY MEASUREMENTS AND CALCULATIONS

During fluid flow, the volumetric flow rate was controlled using calibrated syringe pumps, and the pore-fluid pressure drop across the sample was measured continuously by use of a differential-pressure transducer. An independent check on the uniformity of

volumetric flow rate was provided by an in-line flow gauge. Pressure losses associated with fluid tubing and sintered discs were subtracted from the total measured pressure change. These system losses were established by using a dummy sample with a very large permeability such that essentially all pressure losses recorded corresponded to system losses.

Sample permeability, k_s , was calculated using Darcy's law and the assumption of a linear pressure gradient existing in the sample under steady-state flow conditions. Sample permeability was calculated using

$$k_s = (4 Q \nu L) / (\pi D^2 \Delta P), \quad (1)$$

where Q = volumetric flow rate, ν = dynamic viscosity of pore fluid, L = sample length, D = sample diameter, and ΔP = pressure change across sample. Tabulated values of the viscosity of water as a function of temperature and pressure were assumed to be applicable for the dilute Na_2CO_3 solutions. Flow was assumed to be entirely along the abraded saw cut, but an independent calculation of the "fracture" permeability, k_f , was not possible because the wetted cross sectional area of the fracture could not be measured. Assumption of the parallel-plate model for fluid flow in a fracture allowed calculation of an effective hydraulic aperture, e , of the fracture by the equation

$$e = (3 \pi D k_s)^{1/3}. \quad (2)$$

The parallel-plate model of fluid flow in a fracture predicts fracture permeability to be

$$k_f = e^2 / 12. \quad (3)$$

Use of the parallel-plate model is applicable only when laminar flow within the fracture is distributed uniformly. Should the flow become localized in discrete channels, then the parallel-plate model is inappropriate.

CHARACTERIZATION OF DISSOLUTION-INDUCED SURFACE FEATURES

Surfaces subjected to fluid interaction during a flow-through experiment were examined using both optical binocular and scanning electron microscopy (SEM). Optical microscopy provided an overall view of the general dissolution pattern, whereas the SEM studies provided the microscopic details. The axial saw cut (parallel to basal plane) and the abraded ends of the sample (parallel to m -planes) were studied.

Documentation of the progressive morphology changes utilized overlapping, stereo pairs of SEM images(200x) taken along transects that extended from areas of little dissolution to areas of extensive dissolution. Higher magnification (450x to 1000x), stereo

pairs at selected locations along the transects provided data on the finer details of the surface morphology.

SEM stereo images were obtained using standard techniques. The same area of the surface was imaged with the sample stage at two slightly different orientations relative to the optic axis of the SEM column. One image of the pair was taken with the stage tilted 5° to the left, and the other image was taken with the stage tilted 5° to the right. Most SEM images shown in this thesis are stereo images. Unfortunately, the stereo-image methodology utilized did not permit accurate measurements of the relief of surface elements. Hence, measurement of the inclination of surfaces could not be determined directly from the stereo images.

Quantitative information of the three-dimensional character of the surface was provided by SEM imaging of the surface profile of a section cut normal to the sample axis. One half of the Q2 sample was embedded in epoxy and cut normal to the sample axis with a thin-bladed, diamond saw. The section was carefully abraded and polished with progressively smaller grit sizes in a manner to minimize abrasional edge rounding of the surface profile. The profile was imaged with a Cameca electron microprobe/SEM instrument that had a controlled, positioning sample stage. The center of each SEM image was known to an accuracy of $1\ \mu\text{m}$ relative to a reference datum. This allowed construction of the overall surface profile from a series of overlapping images. This surface profile provided details of variations of surface morphology and the amount of dissolution that occurred along the profile. The edge-profile transect was supplemented with SEM images taken on the reacted saw-cut surface on the other sample half at positions opposite the edge profile. These images allowed correlation of the profile geometries to the corresponding plan view geometries.

PERMEABILITY VARIATIONS WITH TIME

EXPERIMENT Q1

Experiment Q1 primarily was an exploratory experiment to assess the effect of changes of effective pressure and flow rate upon temporal variations of sample permeability. The reactive fluid was a 0.1 M aqueous Na_2CO_3 solution. The experiment consisted of two parts. In part I, the temperature and volumetric flow rate were maintained constant at 125°C and 2 ml/hr, respectively, but the effective pressure was increased incrementally. In part II, the temperature was increased to 160°C and the effective pressure was maintained approximately constant while the flow rate was systematically varied for specific time intervals. In both parts of the experiment, there were time intervals of no flow (rest intervals) associated either with refilling of the in-line reservoir (rest of minutes to an hour) or, on occasion, overnight shut-off of pumps (rest of 5 to 10 hours). In both parts of the experiment, the pore-fluid pressure varied only slightly, ranging from 5.1 to 6.1 MPa (740-890 psi).

At a room temperature of 25°C, the sample permeability was $9.9 \times 10^{-10} \text{ cm}^2$ (100 millidarcy) at an effective pressure of 7.2 MPa (1050 psi). The same permeability was obtained using flow rates of 0.8, 2.0, and 8.0 ml/hr, which validated the use of Darcy's law. For a parallel-plate fracture model and the assumption that all flow is through the axial saw cut, this corresponds to an effective hydraulic aperture of 26 μm and a fracture permeability of $5.6 \times 10^{-5} \text{ cm}^2$.

Part I

The temperature was increased to 125°C under conditions of no flow, then after 10 hours at temperature, flow commenced. The initial sample permeability was $2.9 \times 10^{-10} \text{ cm}^2$ (30 millidarcy) at an effective pressure of 6.9 Mpa (1000 psi). This permeability is only 30% of that of the sample at room temperature at the same effective pressure. Fluid flow was sustained at a constant rate of 2 ml/hr for a net time of flow of 32 hours (excludes rest intervals). The confining pressure and, to a lesser extent, the pore pressure slowly changed during the experiment and were manually adjusted by changing the confining pressure or adjusting the syringe pump rates. In addition to these adjustments, the effective pressure was increased by 6.9 MPa increments at two different times in order to achieve a larger effective pressure.

Figure 9 shows permeability changes as a function of net flow time with rest intervals and effective-pressure changes and adjustments indicated. The permeability data are normalized relative to the initial measurement made at 125°C. The effects of effective-pressure changes largely controlled the major permeability variations. Each increase of the effective pressure was reflected as an abrupt decrease in permeability. In general, the larger the change of effective pressure, the larger the "instantaneous" permeability decrease. The two 6.9 MPa effective-pressure increments induced an instantaneous permeability followed by a time-dependent decrease. Permeability also decreased measurably in conjunction with no-flow intervals of 5 and 9 hours duration. In both cases, permeability did not change immediately before or after the rest period.

During intervals of flow with minimal changes of effective-pressure, the nature of permeability changes varied with net flow time. During the initial 6 hours of flow, permeability increased 40% in an approximately linear fashion. In the subsequent two intervals of constant effective pressure (hours 7-16 and 18-24), the permeability remained constant. Subsequently, during a later interval of constant effective pressure, the permeability decreased slowly with time.

At the end of part I of the experiment, sample permeability was $9.7 \times 10^{-11} \text{ cm}^2$ (10 millidarcy) at an effective pressure of 20.5 Mpa (2975 psi), which is 33% of the initial permeability measured at 125°C and an effective pressure of 6.9 Mpa (1000 psi). After a net flow time of 32 hours, flow was halted and the temperature increased to 160°C over a time of 2.5 hours, while maintaining a constant effective pressure. Part II of the experiment encompassed the 160°C interval.

Part II

In the second phase of the experiment, the effective pressure was maintained approximately at 20.3 MPa and the effect of variation of flow rate assessed. Immediately following establishment of a steady-state temperature of 160°C, the initial permeability was $5.3 \times 10^{-11} \text{ cm}^2$ (5 millidarcy) at an effective pressure of 20.3 MPa (1940 psi), which represents a 55% reduction in the permeability relative to that at 125°C at the same effective pressure.

Temporal variations of permeability were systematic and showed a discernible dependence on volumetric flow rate. For the initial 21 hours of net flow time, the flow rate was maintained at 2 ml/hr. After onset of flow, the permeability decreased slightly during the first hour, then remained constant for several hours and then subsequently increased steadily (Figure 10). During the next 14 hours, intervals of 2 ml/hr flow rate were

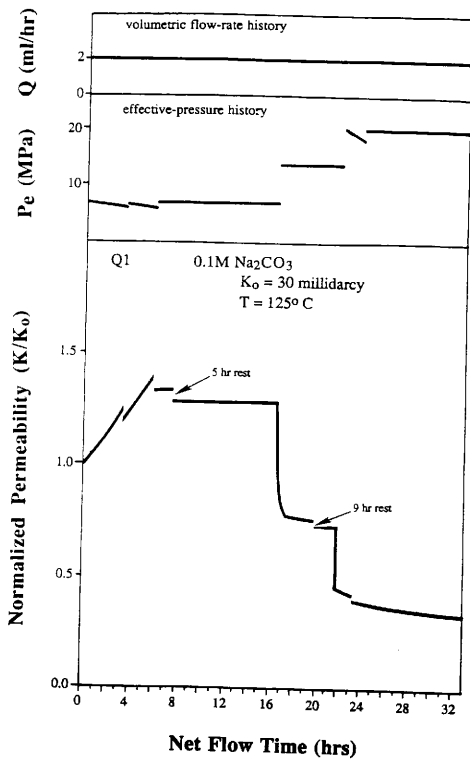


Figure 9. Variation of permeability as a function of net flow time and changes of effective pressure during part I of experiment Q1. Permeability is normalized with respect to the initial value.

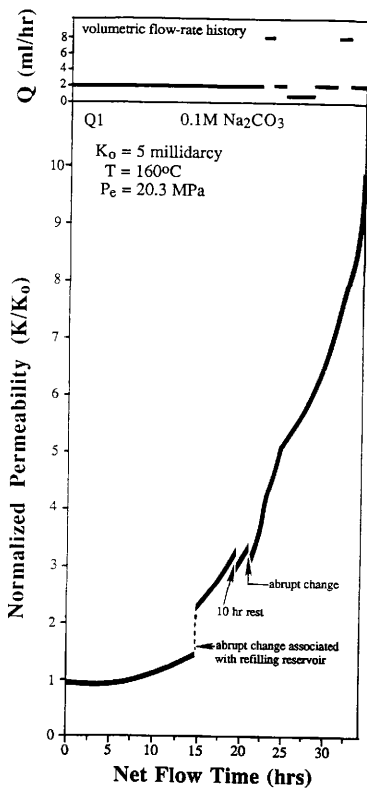


Figure 10. Permeability variation as function of net flow time during part II of experiment Q1. History of volumetric flow rate is shown in upper part of figure.

alternated with intervals of either 8 ml/hr or 0.8 ml/hr flow rate. The permeability progressively increased over time at a rate that depended in part on the flow rate (Figure 10), as indicated by the coincidence of slope breaks and differing slopes of the permeability versus time with differing flow rate intervals. In general, the greater the flow rate, then the greater was the rate of change of permeability for a specific time period in the experiment. If only the 2 ml/hr intervals are considered, one observes the rate of permeability increase escalates with time. This inherent increase of rate with time complicates establishment of a quantitative relationship between flow rate and permeability change. At the end of the experiment, the permeability had increase 10 fold from the initial 160°C value.

Two abrupt permeability changes occurred during the initial 14 hours. A large increase occurred in conjunction with re-filling of the in-line reservoir. Pore-pressure transients associated with opening and closing of valves during the isolation process may have dislodged material that could result in a partial flow blockage along the saw cut. Several hours later an abrupt decrease occurred for no apparent external reason. A permeability decrease also was associated with a 10 hour rest interval.

EXPERIMENT Q2

In contrast to Q1, conditions of experiment Q2 were not varied during the experiment. The temperature and flow rate were maintained constant at 155°C and 2 ml/hr, respectively. The effective pressure varied slowly with time but never deviated more than 1.5 MPa from the average value of 10 MPa. The reactive fluid was a 0.05 M aqueous Na_2CO_3 solution. The initial permeability at temperature was $1.5 \times 10^{-10} \text{ cm}^2$ (15 millidarcy) at an effective pressure of 10 MPa. Assuming the parallel-plate fracture model, this corresponds to an effective hydraulic aperture of 14 μm .

Permeability varied systematically with time (Figure 11). During the initial 17 hours, the permeability slowly decreased and then remained constant for the next 9 hours. Subsequently, the permeability increased at a rate that escalated with time. After 60 hours of flow, the permeability had increased 40 fold. Flow was continued for an additional 17 hours, but the permeability of the sample was sufficiently large compared to that of the flow-system components, such that the sample permeability could not be resolved from that of the flow system.

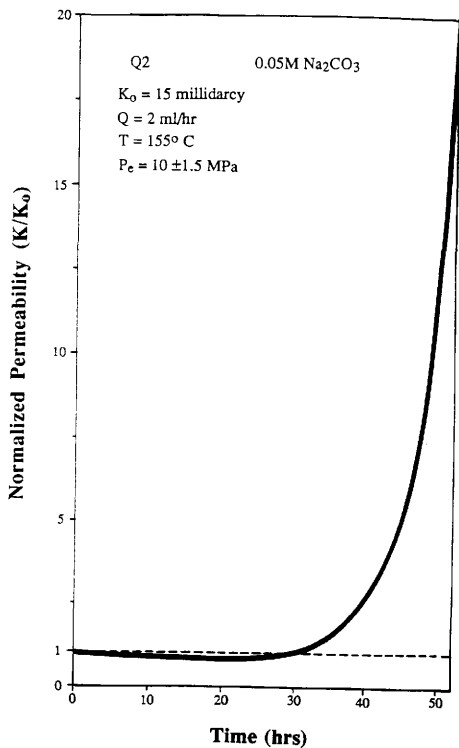


Figure 11. Variation of permeability as a function of net flow time under constant flow rate, temperature and effective pressure. Experiment Q2.

DISSOLUTION MODIFICATION OF ABRADED SURFACES

MACROSCOPIC CHARACTERISTICS

The reacted, axial saw cuts and end sections exhibit systematic spatial variations of surface reflectance as seen either with the unaided eye or under the binocular microscope. Variations of surface reflectivity correlate with differences of surface texture induced by dissolution. On the reacted axial surfaces, several zones of higher reflectance traverse the surface parallel to the flow direction and represent flow channels in which dissolution was most extensive. Both Q1 and Q2 saw-cut surfaces exhibit these channels adjacent the outer edges, but Q2 also has a major centrally positioned channel (Figure 12). Surface reflectance changes transversely across a channel. Each channel can be subdivided in either two or three parallel zones of differing reflectance, although contacts are gradational.

On the Q1 surface, the channeling is restricted to the edges of the saw-cut surface. Channel widths vary from 2 to 5 mm, with the greatest width occurring near the corners. Surface reflectance is greatest adjacent the edge and progressively decreases inwardly.

The saw-cut of the Q2 sample possesses narrow edge channels and a wide axial channel. The edge channels vary in width from 0.5 to 1.5 mm. The central channel is 8 mm wide near the upstream end, enlarges to 12 mm near the midpoint and then narrows to 3 mm adjacent the downstream end. The narrowing of the channel probably reflects a focusing of flow at the downstream end of the sample, because only one sintered disc separated the sample from the endpiece with a small central hole through which the fluid passed. A transverse surface profile of the channel (Figure 13) measured along a section cut at the midplane shows the channel is 70 μm deep near the centerline with the depth decreasing approximately linearly toward the edge of the channel. This confirms the correlation between surface reflectance and extent of dissolution. Within the central channel, surface reflectivity is greatest near the center line and progressively decreases toward the channel margins.

Dissolution also occurred on the ends of the samples. For the Q2 sample, enhanced surface reflectivity is localized in a centrally positioned circular region. Surface reflectivity is greatest near the center and decreases radially outwardly.

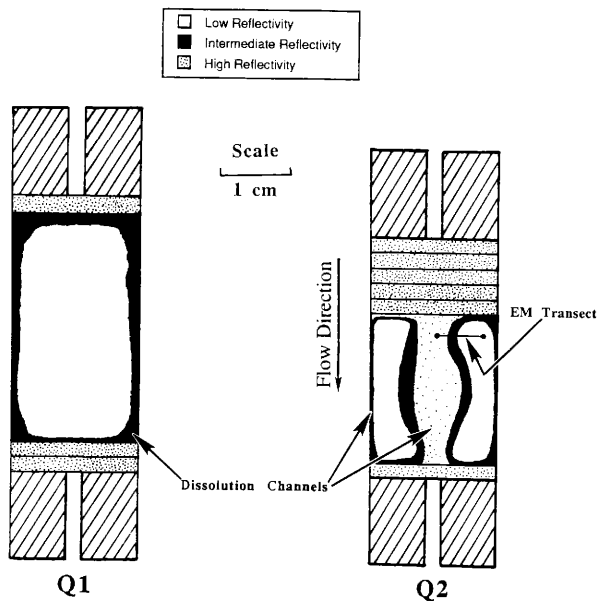


Figure 12. Dissolution channels developed on abraded saw-cut surface of samples Q1 and Q2. Location of SEM transect on Q2 also is denoted.

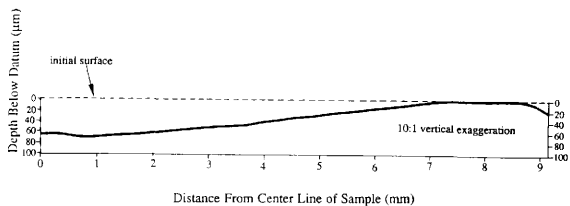


Figure 13. Surface profile across half of the major dissolution channel on sample Q2. Section line extends from the center line to the edge of the sample. Small scale details of the surface profile are smoothed.

MICROSCOPIC CHARACTERISTICS OF REACTED SURFACE

Introduction

The focus of this section is the description of the reacted surfaces of the samples for purposes of characterizing the nature of dissolution modifications. These observations, in turn, form the basis for developing conceptual models for evolution of the forms of both initial surface features and the surface as a whole with increasing dissolution.

Describing the sample surfaces is analogous to describing a land surface. Several different perspectives can be used to describe the surface. For a rugged terrain, one can consider the surface to be comprised solely of either a system of neighboring valleys (concave or "negative" elements) or neighboring ridges (convex or "positive" elements); where the basic building block of the landscape is either a valley element or a ridge element. From this perspective, the surface consists entirely of either negative or positive elements. Alternatively, one can consider the surface to be comprised of a system of alternating valleys and ridges. Use of the latter description has a major drawback, however, because it requires defining where a ridge element ends and a valley element begins. This is not a problem when only a sole type of basic element is used. Ridge lines (drainage divides) separate valley (negative) elements, whereas drainage lines separate ridge (positive) elements.

The single-element approach was adopted for this study. For the initial, unreacted surface, positive elements are considered the basic building blocks. Whereas, for surfaces with discernible dissolution, negative elements are considered the basic building blocks. The basis for these choices will become evident as the surfaces are described. But the choice primarily reflects the nature of the processes affecting development of the surface topography.

Secondary Mineral Formation

Dissolution was the primary process active along the surface, but it was not the sole process. On areas displaying a limited extent of dissolution, SEM images show the presence of a small amount of a secondary mineral that formed during the experiment (Figure 14). On the basis of crystal habit and the chemistry of the solution, the mineral is identified as analcite, $\text{NaAlSi}_2\text{O}_6 \cdot \text{H}_2\text{O}$, which is a framework silicate with a paragenesis compatible with hydrothermal conditions. Johnson (1983) also observed analcite

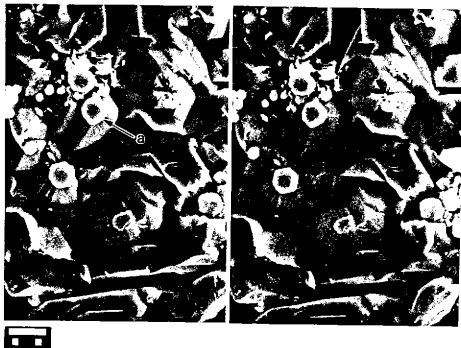


Figure 14. Analcite crystals (a) on reacted surface of Q2. The crystals sit on pedestals formed by dissolution of the quartz substratum upon which they grew. Scale bar equals 10 μm .

formation in his hydrothermal dissolution experiments with Sioux Quartzite and aqueous Na_2CO_3 solutions. Johnson attributed the source of Al to dissolution of a small amount of aluminosilicate minerals, such as kaolinite, in the quartzite. In the present case, the source is not certain. One source is the dissolving quartz itself, because Al^{+3} substitutes for Si^{+4} in quartz. The amount of Al in quartz is only of the order of 0.001 weight percent, which doesn't appear to be sufficient to account for the amount of analcite observed. An alternative source of the Al in these experiments is from contamination of the sintered discs, which had been used previously in a number of flow-through experiments with Sioux Quartzite samples. It is possible that small amounts of kaolinite liberated from the dissolving Sioux Quartzite samples became lodge in the sintered discs, and that the subsequent HCl acid cleaning of the discs was insufficient to purge all aluminosilicate particles from the discs prior to their use in the present experiments.

Details of the spatial distribution of the analcite crystals and their timing of formation are presented in a later section.

SEM Transect

A series of stereo SEM images documents surface characteristics along a transect that extends from an area of indiscernible dissolution to an area of extensive dissolution. The transect is located on sample Q2 on one half of the central dissolution channel (Figure 12). The progressive changes of surface texture observed along the transect provide a record of the evolution of the surface as a function of increasing dissolution, provided the initial population of features affecting dissolution, especially abrasion-induced cracks, was statistically homogeneous along the transect. This assumption is reasonable, considering the cutting and abrasion procedures used on the saw cut.

In contrast with the study of Gratz and others (1990), this study does not track the evolution of the same area with increasing dissolution. Instead, the evolution is established by determining average differences and similarities between neighboring areas with differing degrees of dissolution. These progressive changes are used to infer the evolutionary sequence of specific types of surface elements. In this study, the dissolution *modification of cracks and the evolution of surface elements derived initially from cracks* are of particular importance.

Dissolution modification of the surface as seen along the SEM transect is very pronounced. Figure 15 shows a sequence of SEM images taken along the transect and provides an overview of the changes of surface texture. Figure 16 shows the relative locations of each photo in the overview sequence. Dissolution widening of surface cracks

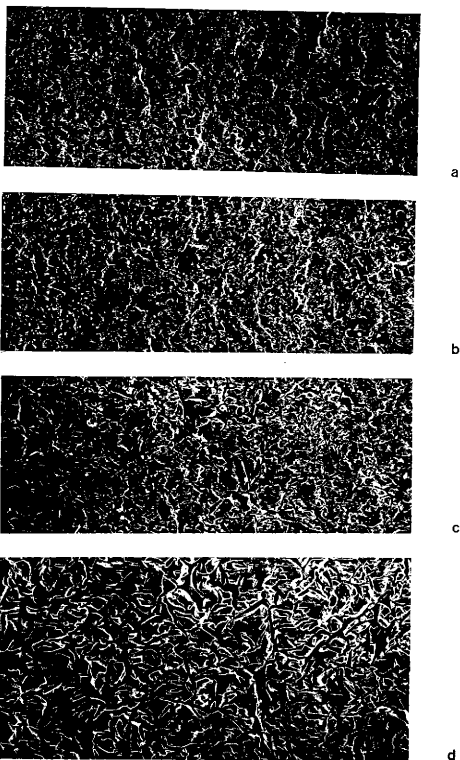
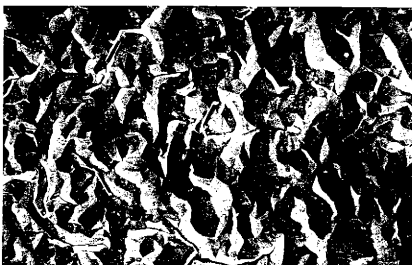


Figure 15. SEM photographs of selected locations along transect showing progressive dissolution modifications of the surface. The extent of dissolution increases from (a) to (g). Location of individual photos on transect is shown in upper part of Figure 16. Scale bar equals 100 μm .



e



f



g



Figure 15. (continued)

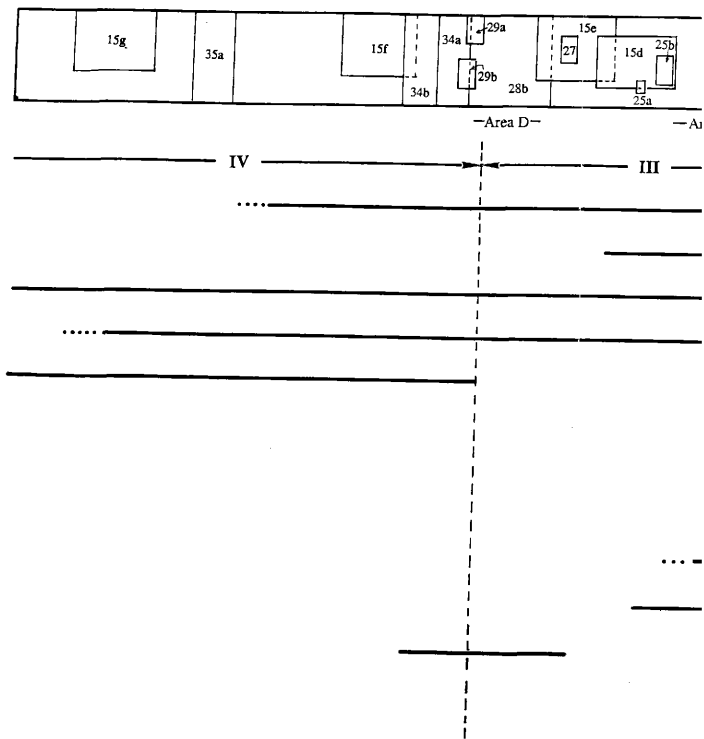


Figure 16. Spatial relations of surface elements on the SEM transect on Q2. Index map at the top shows locat

is readily apparent. In fact, as shown subsequently, dissolution modification of surface cracks is the dominant control on the evolution of the surface texture with increasing dissolution. From a careful study of the SEM images along the transect, five distinctive negative surface elements are distinguished. These negative elements represent dissolution forms derived from initial surface cracks. Furthermore, the spatial relationships between the various dissolution-derived negative elements along the transect indicate that there is an evolutionary sequence in the development of the negative elements. This sequential development, in turn, is used to construct two scenarios for the morphologies of dissolution surface elements associated with dissolution modification of a surface crack.

Subdivision of the transect into five contiguous intervals facilitates presentation of observations. Interval boundaries are distinguished by the first occurrence of either distinct surface elements or features of elements related to dissolution effects. One interval effectively represents the initial unreacted surface, because there are no discernible dissolution effects as determined by a comparison of SEM images of acetate-peel replicas of the original surface with SEM images of the reacted surface. Four additional intervals are identified and are designated by roman numerals.

Figure 16 shows the five intervals and the spatial relationships of various positive and negative surface elements along the transect line. Significant systematic lateral variations of major characteristics of surface elements also are denoted. Figure 16 also shows the locations on the transect line of all SEM images referred to in the text. The orientation of the transect line relative to the crystallographic a-axes is indicated.

Interval of Indiscernible Dissolution

This interval is effectively equivalent to the initial unreacted surface and is assumed to represent the initial condition from which all subsequent intervals evolved. At a macroscopic scale, the original abraded surface of the saw-cut is planar, but at a microscopic scale the surface exhibits an abrasion-induced microtopography. Overall, the surface consists of plateau-like regions with intervening lower areas (Figure 17). Tops of the plateau-like areas are coincident with the planar datum. On average, the plateaus and adjacent lows exhibit different surface textures.

Plateau tops are dominated by fields of small (1-5 μm), closely spaced to overlapping, irregularly-shaped, subrounded asperities (positive elements) (Figure 18), which give the surface an appearance similar to that of a sintered aggregate. Interspersed with these subrounded asperities are a number of small holes of either elongate, polygonal or irregular shape. The origin of the irregularly-shaped, subrounded asperities is uncertain,

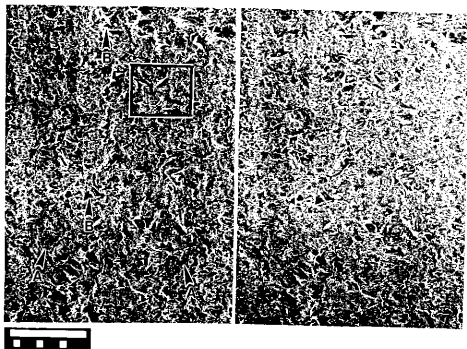


Figure 17. SEM stereo photographs of an area in the interval of indiscernible dissolution. The overall surface topography consists of plateau-like regions (A) coincident with the planar datum and interplateau low areas (B). The area outlined is shown in Figure 18. Scale bar equals 100 μm .

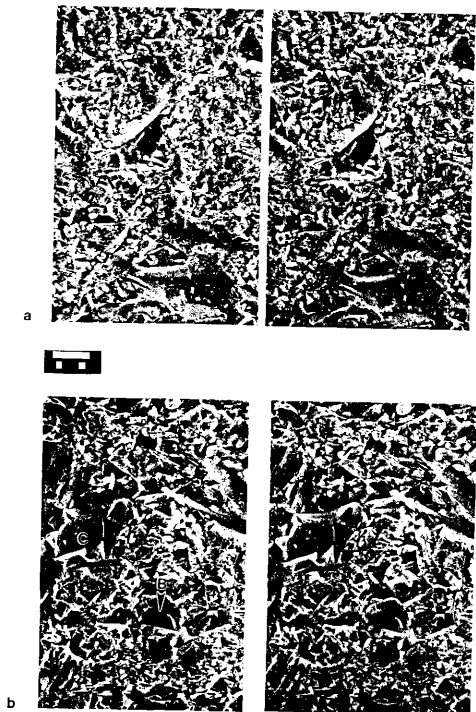


Figure 18. SEM stereo photographs of microtopography of abraded quartz surface in an area of indiscernible dissolution. a) Plateau-like regions (A) with small, rounded asperities. b) Conchoidal fracture surface with ripple marks (B) and interplateau low area (C) with large, angular asperities. Scale bar equals 10 μm .

but they may be a product of intracrystalline plastic deformation associated with loading of earlier formed fracture-induced asperities.

Areas below the planar datum have asperities of varying sizes and shapes that clearly formed as a consequence of abrasion-induced brittle fracture. Surfaces of asperities typically are curvilinear and correspond to exposed crack faces. Asperities often exhibit sharp edges and apices, but a number of asperities exhibit rounded or irregular-shaped edges and apices as a result of abrasional modification of original angular forms. Formation of these asperities is associated with intersection of contact-induced cracks, which form adjacent a contacting abrasive particle, with subsequent removal of quartz fragments. Some exposed crack faces display small-scale ripple or rib marks, which are surface markings related to fracture propagation. Most importantly, exposed crack faces often are associated with cracks that continue further into the interior.

As shown subsequently, the abrasion-induced cracks in the surface layer play the dominant role in the dissolution modification of the surface. Line surveys and census counts of crack intercepts on the surface (SEM images) show crack lengths (surface intercept lengths) vary from 1 to 100 μm with the frequency distribution of crack length highly skewed toward short cracks (Figure 19). Cracks penetrate as deep as 90 μm below the planar datum and commonly follow paths controlled by cleavage as shown by SEM images of the profile section cut perpendicular to the saw-cut. A fracture-mechanics argument can be made for correlating the depth of penetration of a contact-induced crack with the surface intercept length (Brann Johnson, personal communication). Normally, the longer the surface intercept of a crack, the greater is the depth of penetration.

Dissolution Interval I

Occurrence of cracks with discernible apertures marks the first evidence of dissolution (Figure 20). These *etched cracks* have well-defined sharp edges and approximately parallel opposed faces that taper laterally to a relatively sharp tip. Crack apertures are too small to see the deeper parts of the dissolution-modified crack faces.

The span of interval I is small and observed dissolution effects across it are relatively minor (Figure 20). The aperture of etched cracks widen to as much as 0.5 μm . Small rib and ripple fracture-surface markings progressively lose their identity across the interval. The initial sharp edges of asperities become subrounded. On average, the irregular subrounded asperities on plateau tops are slightly more rounded and subdued.

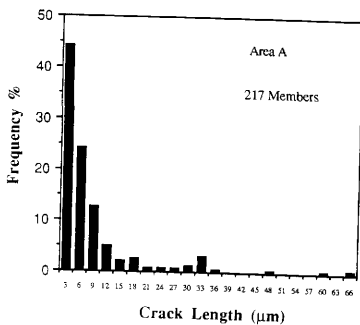


Figure 19. Frequency distribution of length of abrasion cracks in Area A, which is in the interval of indiscernible dissolution.

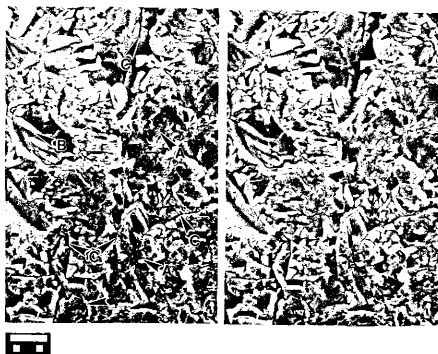


Figure 20. SEM stereo photographs of a representative area on dissolution interval I. Surface modification by dissolution consists of rounding of initial asperities (A) and ripple marks on fracture surfaces (B) and dissolution widening of microcracks (etched cracks) (C). Scale bar equals 10 μm .

Dissolution Interval II

The start of interval II is marked by the first occurrence of two distinctive negative elements not observed on prior intervals. Based on the geometry of their cross sectional profile, these negative elements are referred to as *cusped notches* and *v-shaped notches* (Figure 21). Cusped notches have curvilinear walls that meet at a well-defined axial lineation as seen on a SEM image. V-shaped notches have planar upper walls that typically become curvilinear immediately adjacent the axial lineation that marks the bottom of the element. As first seen, the elements are short ($< 5 \mu\text{m}$), shallow and sparsely scattered across the surface. With increasing dissolution along interval II, the frequency of occurrence and the dimensions of the notches, especially cusped notches, increase measurably. Development of the notches is best on small areas (10×10 to $20 \times 20 \mu\text{m}^2$) with few if any etched cracks (Figure 22a). The v-shaped and cusped notches can occur as isolate individuals, but commonly these elements are interconnected to form branched networks, often with three or four arms (Figure 22a).

On interval II, etched cracks are more evident than on interval I and display some progressive change with increasing dissolution along the interval. Crack apertures progressively widen along the interval, attaining values as large as $3 \mu\text{m}$; although an aperture of 0.5 - $1.0 \mu\text{m}$ is more typical. In addition, lateral terminations of etched cracks more commonly have a blunt form, instead of the sharp tip observed in interval I (Figure 22b).

The smaller asperities and small-scaled fracture-surface markings typifying the initial surface progressively lose their identity across interval II. Small ripple and rib marks on crack faces have been destroyed and only the larger conchoidal fracture surfaces remain identifiable. The fields of small asperities that once dominated the tops of local high areas of the surface become indiscernible with distance across the interval and are replaced by surfaces that are significantly smoother. Cusped notches often occur at these sites. Scattered among these smoother high areas, however, are high areas with a localized anomalous surface texture. These anomalous patches are irregular in outline and the surface has a "corroded" appearance characterized by a distinctive microroughness and small tubules (Figure 22b).

The cusped and v-shaped notches are inferred to evolve from small etched cracks. Qualitatively, one sees a progressive disappearance of very short, shallow etched cracks that is concurrent with the onset and progressive increase of notches of similar dimensions. Frequency distributions of lengths of etched cracks and notches from line-survey samples support this interpretation (Figure 23). Compared to the frequency distribution of crack

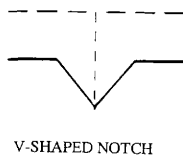
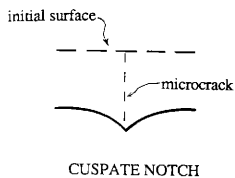


Figure 21. Cross section profiles of cusped and v-shaped notches.

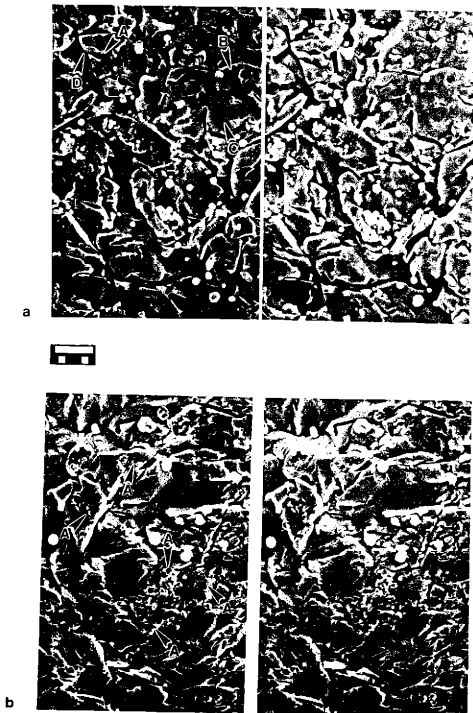


Figure 22. SEM stereo photographs of representative areas in dissolution interval II. a) Individual v-shaped (A) and cusped (B) notches, branched networks of notches (C) and etched cracks (D). b) Areas of anomalous surface texture (A) consisting of a distinctive microroughness and small tubules. Scale bar equals 10 μm .

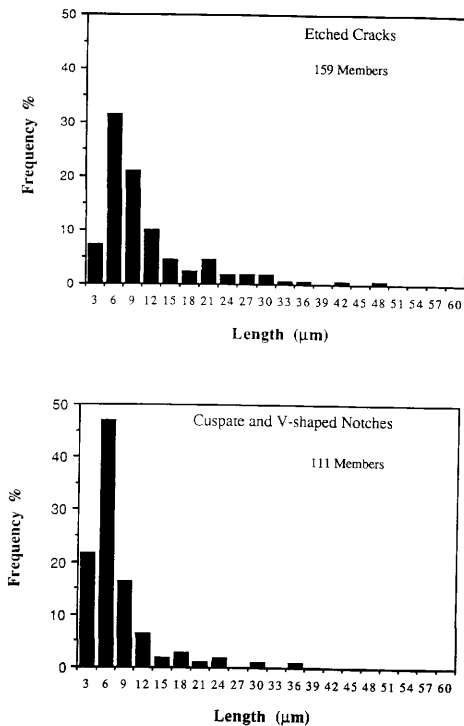


Figure 23. Frequency distribution of the length of etched cracks and cusped and v-shaped notches on Area B in dissolution interval II.

lengths on the initial surface, the sampled etched-crack population has fewer members in the smaller length intervals. This suggests a significant number of cracks with these lengths have lost their identity as a consequence of dissolution modifications. In contrast with the etched cracks, the majority of notch lengths are less than 6 μm . The abundance of notches of sizes coincident with the size of "missing" cracks supports the contention that notches evolve from cracks.

Dissolution Interval III

The beginning of interval III is differentiated by the first evidence of crystallographic control on the morphology and orientation of surface elements. This milestone also closely correlates with distinguishing a new negative element that evolves from an etched crack. The new element is designated a *polygonal widened crack*. Etched cracks, v-shaped notches and cusped notches initially occur in addition to polygonal widened cracks. Crystallographic control on dissolution is manifest by the development of planar slope elements that exhibit a preferred orientation relative to the crystallographic axes. The exact nature of this control varies across the interval in direct relation to the increasing amount of dissolution

The characteristics and progressive changes across interval III of each of the surface elements is summarized below. For presentation purposes, the four basic negative elements are grouped in two pairs. Etched cracks and polygonal widened cracks form one group, and v-shaped notches and cusped notches form the second group.

Etched Cracks and Polygonal Widened Cracks. At the onset of interval III, etched cracks are the dominant negative elements associated with dissolution. Some etched cracks exhibit lateral terminations with a polygonal shape with the edges parallel to the a-axes (Figure 24b). The polygonal nature of the lateral termination becomes more pronounced along the interval (Figures 25 and 27). With increasing dissolution, one or both steep walls often have linear upper edges that are parallel to the a-axes (Figures 27 and 28b). These preferentially oriented, straight edges reflect vertical planar walls of the etched crack that are parallel to a m-plane. By the end of interval III, the density of etched cracks is relatively small.

A polygonal widened crack is differentiated from an etched crack by the morphology of the walls of the element. In contrast with the walls of an etched crack, the walls of the polygonal widened cracks consist of two slope segments: a steeply dipping upper slope and a moderately dipping, lower slope (Figures 26 and 27). The lower slope typically has a slightly curvilinear profile that steepens immediately adjacent a well-defined

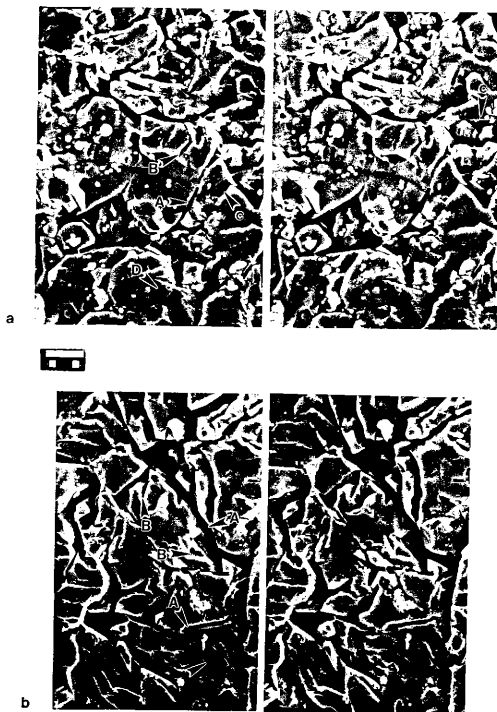


Figure 24. SEM stereo photographs of representative areas of the initial stage of dissolution interval III. a) Examples of etched cracks (A), incipient polygonal widened cracks (B), v-shaped (C) and cusped (D) notches. b) Examples of etched cracks (A), polygonal widened cracks (B) and interconnected branched networks of notches (C). Scale bar equals 10 μ m.

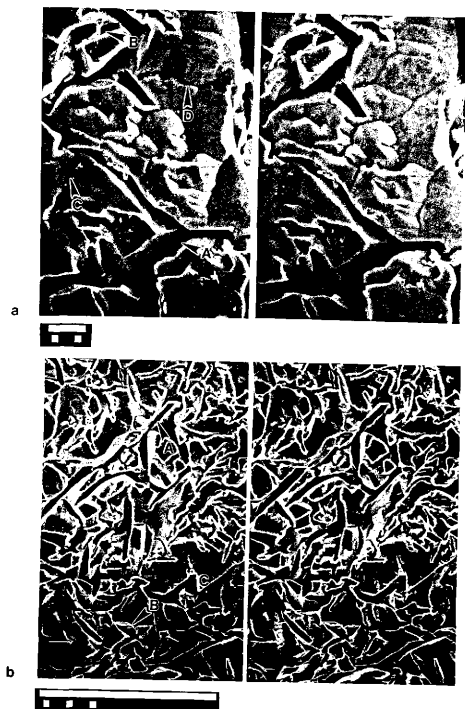


Figure 25. SEM stereo photographs of representative areas of the intermediate stage of dissolution interval III. a) Examples of etched cracks (A), polygonal widened cracks (B), cuspsate (C) and v-shaped (D) notches; scale bar equals 10 μm . b) Lower magnification view of surface showing examples of etched cracks (A) and polygonal widened cracks (B) that bound domains covered with notches (C); scale bar equals 100 μm .

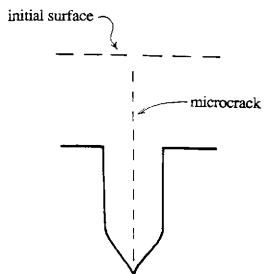


Figure 26. Cross sectional profile of a polygonal widened crack.



Figure 27. SEM stereo photographs of representative area of the advanced stage of dissolution interval III. Microtopography consists of etched cracks (A), polygonal widened cracks (B), and v-shaped notches (C). Scale bar equals 100 μm .

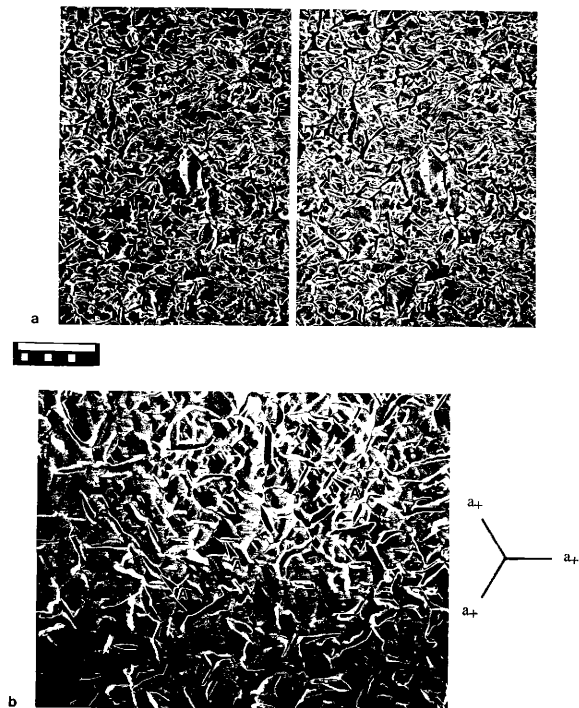


Figure 28. SEM photographs comparing surface modifications along dissolution interval III. a) Stereo pair showing an area of the intermediate stage. b) Area showing the advanced stage in which etched cracks and polygonal widened cracks exhibit a preferred orientation parallel to the crystallographic a-axes. Scale bar is 100 μm .

basal lineation, such that the basal "tip" of the element has a cusped appearance. The change from upper to lower slopes may be gradational or sharp. Some polygonal widened cracks display upper and lower slopes that are further subdivided into a number of planar or curvilinear panels adjoined along a well-defined line (Figures 27 and 29). The edge of the upper slope is sharp and typically is parallel to the edge of the opposed wall except near the lateral terminus (Figures 25, 27, and 29). The paneled character of the upper slope gives the sharp edge of the element a polygonal outline. In some instances, especially with greater amounts of dissolution, the steep upper slopes only partially bound the polygonal widened cracks (Figures 27 and 29). As shown subsequently, variations in morphology of polygonal widened cracks are fairly systematic relative to position on the transect and reflect the degree of dissolution the surface has experienced.

As first seen, polygonal widened cracks are few, short (~5 μm), and poorly developed. With increasing dissolution along the interval, they show systematic changes: (1) their relative abundance progressively increases until attaining a maximum density about midway across interval III and subsequently decreases; as polygonal widened cracks increase in abundance, etched cracks decrease; (2) on average, longer polygonal widened cracks become increasingly more common, which is concurrent with a decrease in the number of the shorter members; (3) the break between the upper and lower slope segments of polygonal widened cracks becomes sharper and the inclination of the lower slope becomes shallower; (4) subdivision of the upper and lower slope segments into panels becomes progressively more common; (5) some panels of the upper wall are vertical and parallel to a m-plane; and (6) polygonal widened cracks only partially bound by steep upper walls increase in abundance.

With increasing dissolution, the aperture of etched cracks and the distance between opposed faces of polygonal widened cracks increase. From a typical aperture of 1 μm in interval II, apertures increase to as large as 20 μm by the end of interval III, although a more typical aperture is about 5 to 6 μm (Figure 30b). Furthermore, by the end of interval III, the aperture of either an etched crack or polygonal widened crack is closely correlated to the length of the element (Figure 31). In general, the longer the etched or polygonal widened crack, the wider is the aperture. Qualitatively, there also appears to be a relationship between element orientation and aperture. In general, elements parallel to a-axes have smaller apertures compared to cracks of comparable length oriented in some other direction (Figure 28).

The length characteristics of the population of etched and polygonal widened cracks change with increasing dissolution. The frequency of short elements decreases across the interval and the frequency distribution for element length becomes progressively less

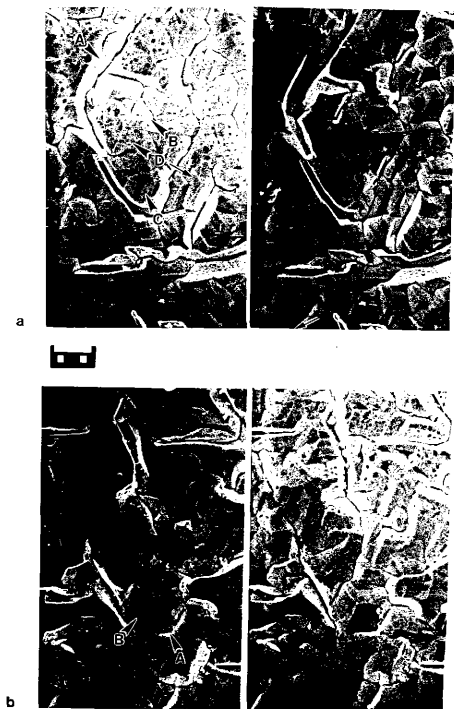


Figure 29. SEM stereo photographs of representative areas of the advanced stage of dissolution interval III. a) Examples of a "paneled" polygonal widened crack (A) and v-shaped notches with (B) and without (C) a cusped tip, and three-sided pyramids (D). b) Examples of v-shaped notches and three-sided pyramids (B). Scale bar equals 100 μm .

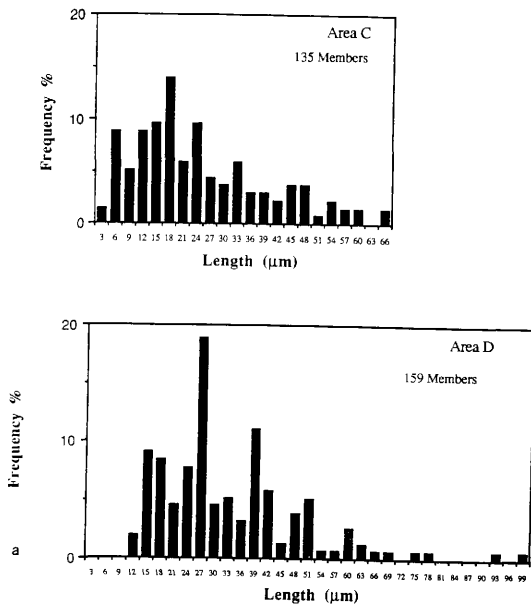


Figure 30. Frequency distributions of the length and aperture of etched and polygonal widened cracks from Areas C and D on dissolution interval III. a) Length distributions for Areas C and D. b) Aperture distributions for Areas C and D.

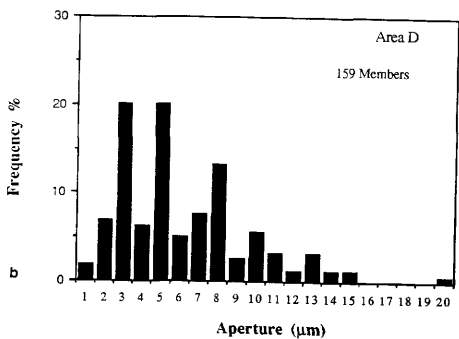
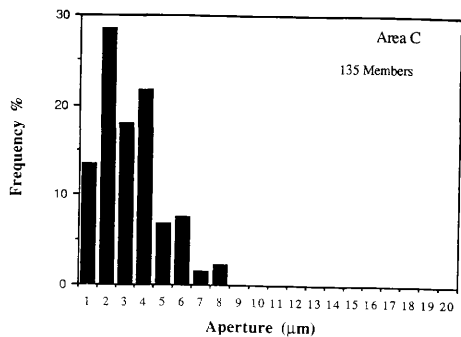


Figure 30. (continued)

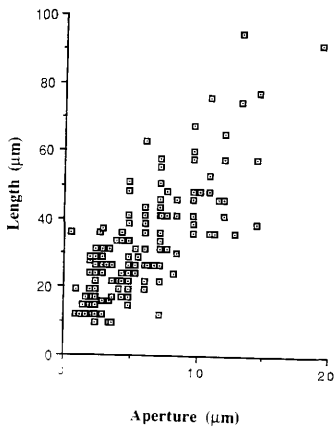


Figure 31. Scatter plot of length versus aperture of etched and polygonal widened cracks in Area D in the advanced stage of dissolution interval III.

skewed toward short members (Figure 30a). By the end of the interval, elements less than $9\ \mu\text{m}$ are not observed and a mean length of an element is of the order of $30\ \mu\text{m}$, which is in contrast with a mean length of $10\ \mu\text{m}$ in interval II.

With increasing dissolution, long axes of etched cracks and polygonal widened cracks exhibit an increasing propensity to be preferentially oriented parallel to a-axes (Figures 28b and 32). This preferred orientation probably does not reflect a direct dissolution effect on element orientation but instead reflects the control of cleavage on the paths of abrasion cracks as they propagated deeper into the abraded surface. It is inferred that the longer cracks tended to propagate deeper and their paths were more strongly controlled by z, r, and m cleavage planes than the shorter, shallower cracks. The preferred orientation of the upper walls of the dissolution widened elements, however, does reflect a crystallographic control on dissolution.

Cusplate and V-Shaped Notches. Cusplate notches greatly outnumber v-shape notches on the initial portion of interval III. Both element types initially are short and shallow and form interconnected branched networks, which usually occur on the higher areas of the surface (Figures 24 and 25). With increasing dissolution, cusplate notches increase in size and relative abundance until attaining a maximum development about midway across interval III. After only a short distance farther, cusplate notches are no longer discernible. V-shaped notches also increase in size and abundance with increasing dissolution and become the dominant element over the latter half of the interval. Over the initial half of interval III, v-shape notches have the typical form described earlier: planar upper walls that merge downward into a cusplate tip, which is marked by a well-defined dark line on the SEM image. Midway along interval III, the planar walls of v-shaped notches start exhibiting a strong preferred orientation. The preferred orientation is demonstrated by the straight, sharp edges formed by the intersection of walls of neighboring v-shaped notches (Figures 27, 28b and 29). The edge is parallel to one of the a-axes. Intersection of the walls of three neighboring, appropriately oriented, v-shaped notches produces a well-defined, three-sided pyramid (Figures 27, 28b, and 29) with edges of intersection that parallel each of the a-axes. The faces of the pyramid are forms of a trigonal dipyrmaid, but the inclination of the faces is too shallow for the planes to be s-planes; the faces appear to be higher-order planes of the form $\{11\bar{2}n\}$, where n appears to be either 2 or 3. Approximately concurrent with the development of these preferentially oriented planes, a modified form of v-shaped notches appears. The planar walls of this modified element extend all the way to a straight, plunging, axial lineation that marks the intersection of the opposed walls; there is no evidence of a cusplate-shaped tip at the axial lineation (Figure 29). Furthermore, the planar walls of these modified v-shaped notches

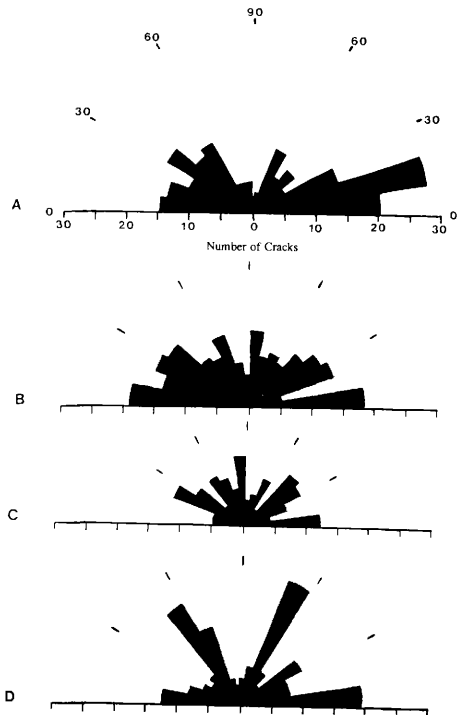


Figure 32. Rose diagrams of the orientation of cracks, etched cracks and polygonal widened cracks in four areas along the SEM transect. The reference direction (0°) is parallel to the SEM transect, which is parallel to an axis. Refer to Figure 16 for the location of Areas A, B, C, and D.

also are preferentially oriented parallel to $(11\bar{2}n)$, as evidenced by the axial lineation paralleling an a-axis. With increasing dissolution, both forms of the v-shape notch increase in length and breadth, such that the three-sided pyramids bounded by three neighboring v-shaped notches become larger with distance along the interval.

Relation Between Polygonal Widened Cracks and V-Shaped Notches.

Several lines of evidence indicate that within interval III most v-shape notches evolve from polygonal widened cracks. Distributions of lengths of etched and polygonal widened cracks show a progressive decrease of shorter members with increasing dissolution (Figure 30a). The length distribution of v-shaped and cusped notches primarily span the size intervals over which the length distribution of etched and polygonal widened cracks is most significantly modified relative to distributions measured on a less reacted area. Compare the distributions from areas B (Figure 23) with areas C and D (Figure 33). The reduced occurrence of shorter etched and polygonal widened cracks matches the increased occurrence of longer cusped and v-shaped notches. The evolution of v-shaped notches from polygonal widened cracks is further supported by the occurrence of polygonal widened cracks missing portions of the steep upper walls (Figures 27 and 29). Sometimes, there is only a vestige of the steep upper slope, and it is usually of a very small height. Loss of identity of the steep upper slope is attributed to lowering of the overall surface to the depth of the more gently inclined lower slope segment.

Relation Between Cusped Notches and V-Shaped Notches. Whether or not cusped notches evolve from v-shaped notches is unclear. The abundance of cusped notches in the initial portion of interval III in which v-shaped notches are substantially less frequent would suggest that cusped notches need not evolve from dissolution modification of a v-shaped notch. In fact, cusped notches appear to be restricted to features of a limited length. Furthermore, the subsequent disappearance of cusped notches midway across interval III suggests that the larger v-shaped notches do not evolve into cusped notches.

Dissolution Interval IV

The appearance of a new negative element, *flat-floored polygonal basins*, marks the beginning of interval IV. The inclined walls of a flat-floored polygonal basin are segmented into a number of planar or curvilinear panels that have well-defined intersections with the floor of the element and adjacent panels (Figures 34 and 35). With increasing distance along the transect, the size and number of flat-floored polygonal basins

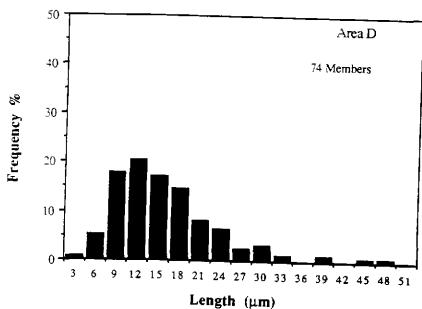
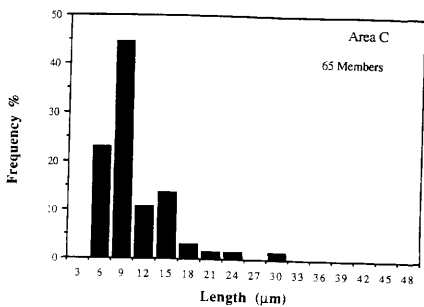


Figure 33. Frequency distributions of the length of cuspsate and v-shaped notches in Areas C and D on dissolution interval III.

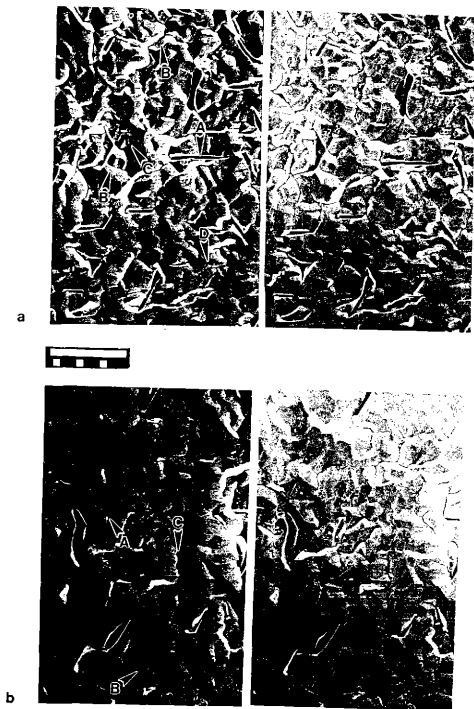


Figure 34. SEM stereo photographs of areas in the initial stage of dissolution interval IV. a) Examples of an etched crack (A), polygonal widened crack (B), v-shaped notches (C) and incipient, elongate, flat-floored polygonal basin (D). b) Slightly more advanced stage showing examples of an elongate flat-floored polygonal basin (A), overlapping and interference between neighboring flat-floored polygonal basins (B) and a complex (paneled) v-shaped notch (C). Scale bar equals 100 μm .

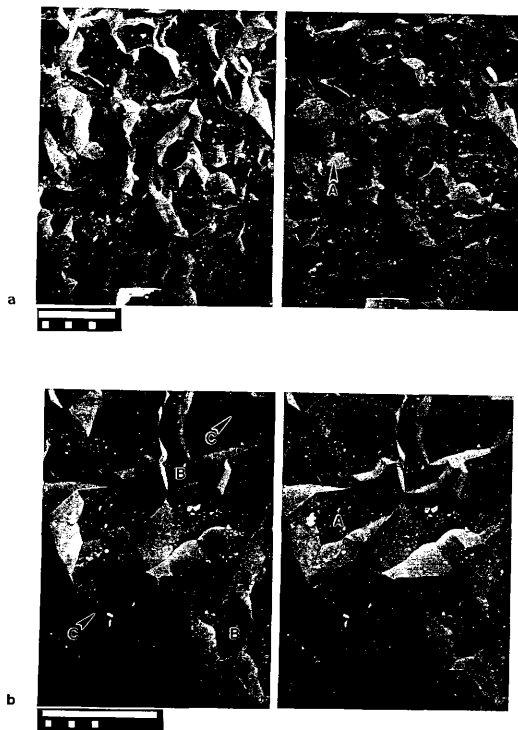


Figure 35. SEM stereo photographs of representative areas in the advanced stage of dissolution interval IV. a) Surface is dominated by irregular flat-floored polygonal basins (A). b) Area of more advanced dissolution compared to (a) showing larger and more regular-shape basins; overlap of neighboring basins results in partial basins (B) and low amplitude, sharp ridges (C).

increase and become the dominant element after only a relatively short distance. As flat-floored polygonal basins increase in prominence, there is a decrease in the areal coverage of v-shaped notches. Etched cracks and polygonal widened cracks become sparser and more widely separated on the surface. It is inferred that these latter elements are associated with the deeper, longer members of the initial crack population.

The first discernible flat-floored polygonal basins are approximately equidimensional and only about 10 μm across. These earliest flat-floored polygonal basins tend to occur on the higher parts of the surface scattered among fields of v-shaped notches. A short distance farther along the transect, both equidimensional and elongate flat-floored basins occur. At this stage, the elongate basins with narrow floors usually are longer and the floor positioned deeper than equidimensional basins in the immediate vicinity. With increasing dissolution, the elongate polygonal basins become more equidimensional with wider floors but the walls do not appear to significantly change inclination. This implies that widening of elements occurs by parallel retreat of the walls. In the early stages of their development, polygonal basins are of an irregular form and the panels of the walls do not display a prominent preferred orientation. With increased widening, however, the basins acquire a more regular polygonal form and wall panels are more preferentially oriented (Figure 35).

Widening of polygonal basins by parallel retreat of the walls results in neighboring polygonal basins intersecting one another. The nature of the "interference" of one element on another depends primarily on the relative depths of their respective floors. If the floors are of similar depth, overlapping of the domains of the elements first produces a sharp-edged v-shaped ridge between the elements (Figure 35). With continued widening of the neighboring elements, the divide evolves into a sharp-edged, low amplitude, cusped ridge that separates adjoining gently concave-upward floors (Figure 35). This scenario contrasts with that of two interfering elements with differing floor depths. In this case, the basin with the greater depth progressively consumes its shallower neighbor so that the latter is only a partial polygonal basin (Figure 35). With sufficient widening of the deeper basin, the shallower neighboring basin is completely annihilated.

Initially, v-shaped notches are the dominant elements on interval IV. Overlap of domains of neighboring v-shaped notches produces the distinctive three-sided pyramids described earlier as a consequence of the strong preferential orientation of the planar walls of v-shaped notches at this stage of dissolution modification of the surface. With increasing dissolution along interval IV, v-shaped notches become longer, the axial lineation is segmented and adjoining walls are subdivided into planar or curvilinear panels (Figure 34). The intersection of walls of neighboring larger v-shaped elements does not

result in either the prominent three-sided pyramids seen earlier in the interval or other preferentially oriented straight edges. This implies that the panels of these larger v-shaped notches are less preferentially oriented compared to the planar walls of the shorter, less complex v-shaped notches.

Conceptual Evolution Scenarios for Dissolution Modification of Cracks

The five distinct negative elements are interpreted to represent different stages in the dissolution modification of an initial surface crack. Based upon the systematic spatial relationships between the different elements, two different scenarios are proposed for the evolution of a crack on a surface approximately normal to the c-axis of quartz. The initial dimensions of the crack appear to influence the morphology of the dissolution form. Cracks with a shallow depth of penetration appear to exhibit a different sequence of dissolution modifications than do deeper penetrating cracks. The conceptual models presented below show two inferred scenarios of the evolution of a steeply dipping, surface crack sufficiently far from a neighboring crack such that dissolution forms of neighboring cracks do not overlap spatially. Clearly this is not the case on an actual surface where interference effects due to overlap of evolving dissolution forms occurs. The emphasis here is on the inferred form of a dissolution-modified crack in the absence of interference effects. The role of overlap of dissolution forms of neighboring cracks on the evolution of the overall surface texture is discussed subsequently.

Constraints on dissolution in the immediate vicinity of the crack tip appear to exert an important control on the form of a dissolution-modified crack. As dissolution widens a crack by lateral migration of the exposed "faces", the position of the crack tip appears to be fixed or "pinned" spatially until the dissolution surfaces adjacent the crack tip have acquired a planar geometry, often with specific crystallographic orientations. At this stage one of two events occurs. Either the line of intersection of the opposed planar faces migrates laterally in direct relation to migration of the adjacent walls or the former crack tip is replaced by a planar or curvilinear surface that displaces downward in parallel fashion with increasing dissolution. The role of the crack tip on controlling the morphology of the dissolution form of a modified crack appears analogous to the role of the tip of a line dislocation on the evolution of etch pits as reported by Joshi and Vagh (1968) and summarized in a previous section. In the latter case, as dissolution increased, a "point bottomed" etch pit transformed into a "planar bottomed" etch pit.

Crystallographic controls on dissolution in quartz affect the evolution of dissolution-modified crack in several ways. The rate of dissolution normal to the plane of

the saw cut relative to surfaces inclined to the saw cut is an important factor. Gratz and others (1990) suggest the differential rate of dissolution of the fastest and slowest dissolving planes in quartz in a moderate alkaline solution is of the order of 5 times. This suggests the dissolution rate normal to the basal saw cut should be at least several times greater than dissolution normal to m-planes, which is the slowest dissolving plane. In the scenarios presented below, the rate of dissolution parallel to the c-axis (normal to saw cut surface) is assumed to be three times that of the m-plane.

Scenario I. Shallow cusped notches are most common on surfaces with limited dissolution and appear to be the last stage of evolution of shallow cracks. In contrast with deeper penetrating cracks, shallow cracks appear not to possess a sharp upper edge as the faces of the crack are dissolved. Instead, shallow cracks widen by a progressive laying back of the faces and rounding of the upper edge (Figure 36a). The overall profile of the modified crack is that of a cusped notch. With increasing dissolution the overall surface is lowered and the relative relief across the cusped notch decreases. Once the overall surface has been lowered to the depth of the initial crack tip, the last vestige of the very subdued cusped notch is destroyed. The v-shaped notch may be an intermediate stage in the evolution of some shallow cracks, especially those members near the upper end of this size interval. It is estimated that cracks that penetrate as deep as 10 μm will evolve with dissolution according to scenario I.

Scenario II. Cracks that penetrate greater than about 10 μm follow a different evolution sequence (Figure 36b). The etched crack is the initial dissolution stage and entails an approximate parallel retreat of the opposed faces of the crack. The faces of the etched crack taper toward the crack tip, and the upper edge of the widened crack adjacent the upper surface is sharp. With increasing dissolution, the etched crack aperture widens and eventually takes on the form of a polygonal widened crack, which is characterized by the segmentation of the dissolved crack faces into two slope segments: an upper steep segment and a shallower dipping, curvilinear segment. The upper edges of the polygonal widened crack are sharp. The lateral crack tips evolve into polygonal forms with segments parallel to m-planes. With increasing dissolution the steep upper walls of the polygonal widened crack migrate laterally and tend to become parallel to m-planes. The slope break between the upper and lower slope segments becomes sharper and the dip of the lower segment progressively decreases as the aperture of the polygonal widened crack increases. With increasing dissolution the faces of the polygonal widened crack segment further into a number of panels. Dissolution normal to the saw cut lowers the overall surface, such that the height of the steep upper slope segment decreases with increasing dissolution. Eventually, lowering of the upper surface is sufficient to remove all evidence

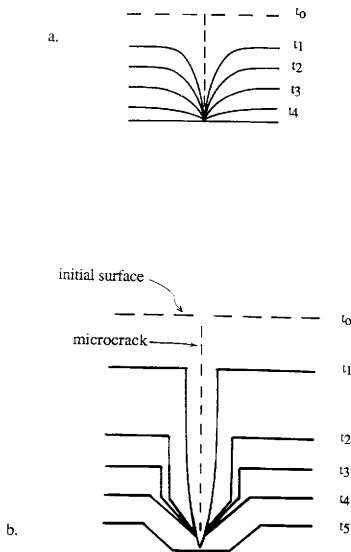


Figure 36. Conceptual models of the dissolution-induced evolution of a surface microcrack. Figure shows sequence of surface profiles at differing times after onset of dissolution. a) Scenario I corresponds to evolution of cracks that penetrate less than $10\ \mu\text{m}$. b) Scenario II corresponds to evolution of cracks that penetrate deeper than $10\ \mu\text{m}$.

of the earlier existing steeper upper slopes. A v-shaped notch negative element represents the subsequent stage in the evolution scenario. Walls of v-shaped notches continue to lay back and the planar segments adjacent to the cusate tip tend to acquire a preferred orientation parallel to $\{11\bar{2}n\}$, where n appears to be either 2 or 3. Once this preferred orientation of the planar slopes is achieved, the planar walls retreat in a parallel fashion. Ultimately, this results in replacement of the cusate tip by a v-shaped tip formed by the intersection of opposed planar slopes.

The modification of the cusate tip of a v-shaped notch into a v-shaped tip marks the onset of the next stage of evolution with the development of flat-floored, polygonal basins. The axial lineation of the v-shaped notch is replaced by an enlarging planar to gently curvilinear surface with sharp intersections with bounding planar to curvilinear walls. The walls retreat approximately in a parallel fashion, although there is a tendency for the walls to acquire trends parallel to preferred crystallographic directions. Dips of the walls are between 25° and 35° and appear to remain approximately constant as a polygonal basin enlarges.

The dimensions of a surface crack determine the dissolution form associated with the crack after a given amount of dissolution. The longer and more deeply penetrating a crack, the greater the volume of material that must be dissolved in order for the crack to achieve a specific stage in the evolution of dissolution forms derived from surface microcracks. This relation between the amount of dissolution, the stage in the evolution of dissolution elements derived from cracks, and the initial crack dimensions plays an important role in understanding the dissolution-induced evolution of the overall morphology of an abraded surface containing a population of microcracks.

Evolution of the Overall Surface Texture with Increasing Extent of Dissolution

Understanding the evolution of the surface texture with increasing dissolution is tied intimately to knowing the evolution scenarios of the dissolution surface elements derived from cracks and appreciating the role of "interaction" between nearest-neighbor dissolution elements with an increase of the extent of dissolution. Interaction between neighboring elements occurs when there is overlap of the areal extent of the individual elements. The areal extent of an element, in turn, reflects both the initial dimensions of the microcrack and the dissolution form to which the crack has evolved. The shallower, shorter cracks evolve into dissolution elements with smaller areal extents than the dissolution elements derived from deeper, longer cracks, which are at a similar dissolution

stage. The spacing between the initial microcracks determines the amount of dissolution required for their associated dissolution elements to widen sufficiently to intersect neighboring elements. The greater the spacing between cracks, the greater the amount of dissolution required before walls of neighboring elements intersect.

Once intersection of neighboring dissolution elements occurs, the nature of the subsequent "interaction" depends upon the depths of the elements relative to a common datum and the nature of motion of the walls of the elements with increasing dissolution. Depths of neighboring elements may be similar or significantly different. For the former case, continued "laying back" or lateral migration of the walls of the elements results either in a mutual annihilation of the elements or the merger of the two smaller elements into one larger, composite element. A "laying back" of the walls favors the former scenario, whereas a lateral, parallel retreat of walls favors the latter case. When there is a significant difference of depth of neighboring elements, the shallower element is annihilated by the lateral or downward movement of a wall of the widening, deeper element; the deeper element remains discernible, although possibly with a modified form. The depth of the crack tip determines either directly or indirectly the depth of dissolution elements derived from cracks.

The above inferences indicate that the distributional forms of the length, depth and spacing of surface cracks influence the evolution of the texture of the overall surface with increasing dissolution. In the present study, as noted earlier, the abraded quartz surface contained an initial population of microcracks with a distribution of crack lengths highly skewed toward short cracks (Figure 19). Furthermore, it was inferred that the depth of penetration of the cracks correlates to the depth of penetration; on average, the longer the crack, the greater is the penetration depth. The observed distribution of crack lengths also implies that the spacing between cracks of similar length, hence depth of penetration, is greater, the longer is the crack (Figure 37a). These dimensional and spatial details of the microcrack population are manifest in the observed evolution of the overall surface texture. A conceptual model for the evolution of the dissolved abraded quartz surface is presented below and shown schematically in Figure 37, which shows a sequence of profiles of the same surface segment subjected to increasing amounts of dissolution.

In the early stages of dissolution (dissolution interval II and the early stage of dissolution interval III) all microcracks exhibit dissolution modifications, but changes associated with the smaller cracks are especially important relative to interaction between neighboring dissolution elements. The shorter, shallower cracks transform into cusped notches (Figure 22a) with walls that "lay back" with increasing dissolution (crack-dissolution scenario I shown in Figure 36a). The spacing between these elements is small

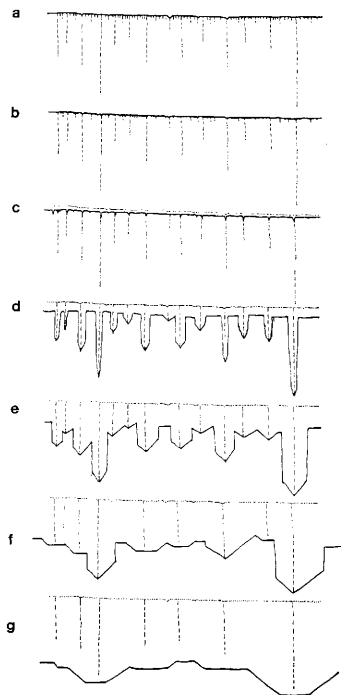


Figure 37. Conceptual model for the dissolution-induced evolution of the surface of quartz with an initial population of microcracks. The initial surface is denoted by dots, and the initial microcracks by dashed lines.

and overlap of the areal extent of elements is common. Where neighboring cusped notches of similar depth overlap, one sees positive elements composed of walls of the intersecting cusped notches. The positive elements appear as low amplitude, convex mounds outlined by the dark, straight or curved lineations that mark the location of the crack tips associated with the cusped notches. With increasing dissolution, the walls of the intersecting cusped notches progressively decline and the intervening high eventually disappears (Figure 37c); this marks the mutual annihilation of the overlapping cusped notches. This scenario occurs for progressively larger cusped notches associated with somewhat longer, deeper cracks that are wider spaced. With the demise of the last vestiges of the cusped notches, areas once containing small groupings of cusped notches have a gently undulatory appearance. These locally "smooth" areas commonly occur on the higher areas of the surface, on local portions of the original "plateau-like" regions, where small, closely spaced microcracks were especially common. These local areas are bounded by dissolution elements derived from larger members of the microcrack population. At this stage, dissolution surface elements associated with the shorter, shallower cracks have disappeared (Figure 37d).

With increasing dissolution, the dissolution elements associated with progressively longer and deeper members of the crack population evolve following scenario II (Figure 36b) achieving intermediate to advanced forms and intersect neighboring elements. The typical interacting elements are either v-shaped notches or polygonal widened cracks. Interaction between v-shaped notches is especially common from the advanced stage of interval III through the early stage of interval IV (Figure 37e). Intersection of v-shaped notches having planar slopes preferentially oriented parallel to $\{11\bar{2}n\}$ gives rise to linear ridges aligned parallel to an a-axis. An oriented, three-sided pyramid develops as a consequence of the intersection of three neighboring v-shaped notches with preferentially oriented walls (Figures 27 and 29). If there is a significant difference of the depth of the intersecting v-shaped notches, then the shallower notch may eventually be consumed by the deeper notch. By this means, v-shaped notches occurring on an area become progressively less numerous but larger, on average, with increasing dissolution. Dispersed throughout the v-shaped notches are etched cracks and polygonal widened cracks that represent the dissolution elements associated with the longer and deeper members of the initial microcrack population.

With increasing dissolution, v-shaped notches with cusped-tips escaping annihilation evolve into v-shaped notches devoid of the cusped tip (Figure 29). This is a critical stage marking the onset of development of a flat-floored element. These flat-floored polygonal basins widen and deepen by parallel migration of the walls and floor. The earliest basins are small and appear to be short lived because they are surrounded and

ultimately consumed by widening of deeper, v-shaped notches and polygonal widened cracks. Eventually as deeper v-shaped notches achieve the critical state for development of flat-floored basins, the number of basins increases until they become the dominate type of surface element.

In a fashion similar to the interaction between v-shaped notches, the widening and deepening flat-floored polygonal basins interact with their neighbors (Figures 34 and 37f). Shallower v-shaped notches and flat-floored basins are annihilated progressively by the deeper basins. With increasing dissolution, the progressive widening and deepening of basins is effectively the sole process occurring with the shallower basins being dissected and eventually eliminated. Ultimately, a small number of large basins comprises the surface texture (Figures 35 and 37g). These basins are associated with the longest and deepest members of the initial microcrack population, which is restricted to be in a layer about 100 μm thick. There appear to be no intracrystalline microcracks in the single crystal used, hence dissolution lowering of the surface does not expose additional microcracks to act as dissolution nuclei. This would not be the case for many naturally occurring mineral grains in rocks, because these grains commonly contain intragranular microcracks and partially healed microcracks associated with a prior deformation history.

Although the surface evolution model described above is for the specific case of an abraded quartz surface, there are several important aspects that should be common to the dissolution-induced surface-texture evolution of other quartz surfaces, provided microcracks are the dominant dissolution nuclei. Differences in the distributional forms of the dimensions and spacing of the microcrack population will control the details of the evolution of the surface with increasing dissolution. The spacing between cracks and the depth of crack penetration below the reacting surface appear to be particularly important parameters.

Within the context of the above inferences, the evolution of dissolution-induced surface texture on a naturally occurring macrofracture in a quartzose rock will depend upon the prior deformation history of the mineral aggregate, the nature of origin of the macrofracture, and its post-formation deformation history. All these aspects are important because they influence the microcrack population at and adjacent to the macrofracture surface. For example, the dissolution surface of a pristine tensile macrofracture will differ from that developed on a macrofracture experiencing a component of shear displacement. This difference was seen in the studies of Johnson (1983), who dissolved both tensile fracture and polished, abraded surfaces of Sioux Quartzite. The dissolution surfaces differed most notably in the early stages when the surface texture of the polished abraded surface was dominated by dissolution modification of abrasion-induced microcracks in a

thin surface layer. Not until the surface layer containing abrasion cracks had been dissolved away and the typical intragranular microcrack population in the quartz grains was exposed did the reacted abraded surface look similar to that of the reacted tensile fracture. At this stage, the microcrack populations controlling dissolution modification of the surface are identical.

Comparison Of Surface Textures of A Reacted Abraded M-Plane And Basal Plane

The abraded ends of sample Q2 are parallel to an m-plane and exhibit dissolution that decreases radially from a maximum intensity adjacent the central edge of the saw cut. A 4 mm long SEM transect, starting at the center of the saw-cut edge and oriented parallel to the c-axis, was studied for purposes of a comparison with the reacted abraded basal plane (axial saw cut). Figure 38 shows stereo photographs of areas at the ends of the transect. The surface of the least dissolved area (Figure 38a) is comprised of polygonal widened cracks and steep-walled, irregularly-shaped, flat-floored basins; some flat-floored basins look like polygonal widened cracks but with flat floors. The steep upper edges of the polygonal widened cracks and basins are preferentially oriented parallel to and at 45° to the c-axis. If the walls of the elements are perpendicular to the m-plane, the oriented edges represent the intersection of a-planes $\{11\bar{2}0\}$ and s-planes $\{11\bar{2}1\}$ with the m-plane.

With increasing dissolution, polygonal widened cracks transform into flat-floored polygonal basins. Initially, the polygonal basins are elongate and irregular in form but progressively acquire more equidimensional dimensions and more regular forms. During this transformation, walls of basins are usually planar and appear to trend parallel to either m-, r-, and z-planes. With still greater dissolution, many basins become rectangular in form with their long axes aligned either parallel to or perpendicular to the c-axis (Figure 38b). The rectangular basins have two walls parallel to an m-plane with the other two walls parallel to a r- and z-plane, respectively. The rectangular form is similar to that noted by Gratz and others (1990) on reacted m-planes, but they noted a consistent alignment of the long axis parallel to the c-axis. As on the abraded basal surface, interaction between neighboring polygonal basins determines the evolution of the surface in the advanced stage of dissolution. The only major difference between the surface texture of the reacted m-plane and the basal plane is the differing crystallographic control on basin geometry as a consequence of the different orientation of the overall surface relative to the crystallographic axes.

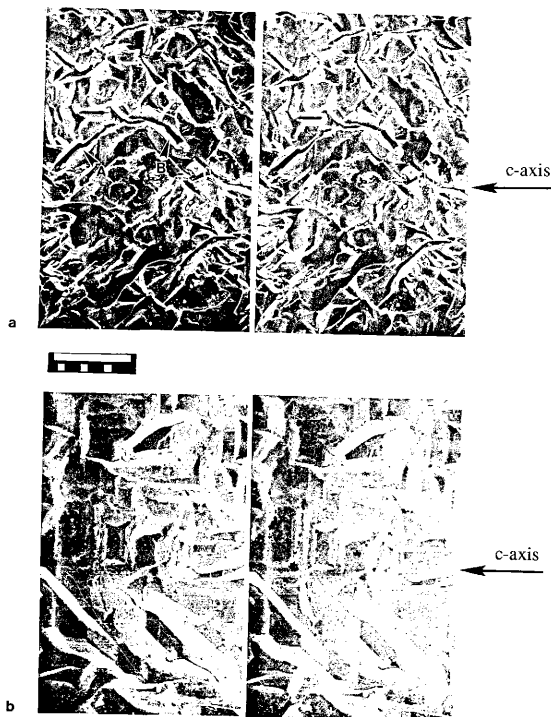


Figure 38. SEM stereo photographs of two areas along the transect on the upstream end of sample Q2. The sample end is parallel to a m -plane. a) Less advanced stage of dissolution showing polygonal widened cracks (A) and steep-walled, flat-floored, polygonal basins (B). b) More advanced stage of dissolution showing several forms of flat-floored polygonal basins; the rectangular basins are especially prominent at this stage. The arrow shows the orientation of the c -axis. Scale bar is equal to 100 μm .

RELATIONSHIP BETWEEN PERMEABILITY CHANGES AND DISSOLUTION-INDUCED SURFACE MODIFICATIONS

The nature of the permeability experiments limit what can be deduced about the details of dissolution-induced changes of permeability, but several key deductions are permissible. Two aspects of the temporal variation of fracture permeability of experiment Q2 are addressed: (1) the initial interval in which the permeability slowly decreased and then remained constant and (2) the subsequent increase of permeability at an ever escalating rate.

The slow decrease of permeability is attributed to either or both of two possible mechanisms. One mechanism is associated with formation of the secondary analcite crystals, and the other mechanism is associated with time-dependent closure of the fracture as a consequence of processes acting at the load-bearing asperities. Processes affecting the load-bearing asperities could be pressure solution or time-dependent, chemically-enhanced fracture (stress-corrosion fracture).

The timing of formation of the analcite appears compatible with it affecting permeability early in the experiment. Where analcite crystals are observed in areas of discernible dissolution, they invariably rest on pedestals formed by dissolution of the quartz substratum upon which the crystals grew (Figure 14). Furthermore, analcite crystals are only observed on those parts of the surface with a limited amount of dissolution. On the SEM transect, the greatest density of analcite crystals occurs on dissolution interval II and the last evidence of analcite crystals is seen in the earliest stage of interval III in the form of isolated pedestals without analcite "caps" (Figure 16). These observations appear most consistent with the crystals initiating prior to occurrence of significant dissolution. The formation of analcite crystals in the "fracture aperture" would decrease permeability as a consequence of the reduction of the wetted cross-sectional area of the fracture. In principle, the reduction of permeability by precipitation of a secondary mineral is directly related to the volume of secondary product in the fracture. So if one knows the density and size of the "blocking" particles, one can estimate the associated reduction in permeability.

The role of a process such as pressure solution at load-bearing asperities cannot be ruled out as a possible cause of slow permeability decrease. Nevertheless, the only evidence suggestive of the occurrence of pressure solution is associated with small areas of anomalous surface texture located on the transect in dissolution interval II (Figure 22b). The anomalous areas occur on the higher parts of the local surface and display a morphology atypical of surrounding areas. The anomalous areas exhibit a "worm eaten" or

"corroded" appearance. This distinct texture may result from pressure solution, although the proof is weak. The strongest support comes from observations reported by Johnson (1983), who shows SEM photographs of areas on Sioux Quartzite that had been locally loaded by quartz sand grains transmitting an effective normal stress in the presence of a chemically-reactive fluid.. The surface texture of these stress-supporting areas looks similar to the anomalous areas seen on the reacted saw cut, looking areas.

The available data are not adequate to differentiate between the two mechanisms for time-dependent permeability decrease. Clearly, additional experiments are needed to resolve the above uncertainty. Elimination of formation of secondary minerals is essential, if the possible role of pressure solution or other process affecting load-bearing asperities is to be determined.

The observed increase of permeability at an ever escalating rate is most readily correlated with the development of the dissolution channels. The localization of dissolution in discrete channels results in a fluid flow short circuit such that the flux of reactive fluid is no longer approximately uniform along the fracture. The development of the dissolution channels results from a positive-feedback mechanism between fluid flux, fluid residence time in the fracture and the average local dissolution rate. The average local rate of dissolution of quartz is related to the degree of undersaturation of the fluid adjacent to the surface. The greater the degree of undersaturation, then the greater the dissolution rate, all other factors being constant. The local degree of undersaturation depends upon the net time of reaction of the fluid since it entered the fracture. The longer this time, the lower is the degree of undersaturation and the slower is the local dissolution rate. The upstream history of fluid flux determines the net time of reaction prior to the fluid reaching a given location along the fracture. The greater the average flux of the fluid, the shorter the net reaction time. For a constant hydraulic gradient, the fluid flux depends upon the spatial variation of the aperture of the "flow channel" followed by the fluid. If the fluid follows a local high conductance path, the average dissolution rate along the local channel will be higher than compared to different lower conductance paths followed by neighboring fluid packets. Consequently, a greater amount of quartz is dissolved along the local high conductance path, which in turn results in a greater conductance because of the increased hydraulic aperture, which provides a further enhancement of dissolution and so on in an escalating fashion. In the experiments, volume flow rate was kept constant. Hence, once a flow channel of significantly higher conductance is formed from one end of the sample to the other, flow is short circuited through the channel and the driving force for fluid flow in the areas of the fracture with a smaller hydraulic aperture is significantly decreased. This, in

turn, results in slower local fluid fluxes such that less dissolution occurs along these regions of the fracture.

The development of discrete dissolution channels that focus the flow in the fracture indicates that the applicability of the parallel-plate model of fluid flow in fractures may be limited to only the early stages of flow entailing dissolution reactions. Once significant flow channels form, the assumption of uniform flow associated with the parallel-plate model is invalid.

MAJOR OBSERVATIONS AND CONCLUSIONS

TEMPORAL VARIATIONS OF FRACTURE PERMEABILITY AND THE RELATION TO DISSOLUTION EFFECTS

The permeability of an abraded saw cut aligned normal to the c-axis of a quartz crystal changed systematically during sustained flow of a dilute aqueous sodium carbonate solution under conditions of constant volumetric flow rate (2 ml/hr), temperature (155°C), and effective pressure (10 MPa). The permeability slowly decreased during the initial 25 hours and then increased progressively at an ever escalating rate. After 60 hours of net flow time, the permeability was 40 times larger than the initial value. The increase of permeability results from dissolution widening of the macrofracture, but the dissolution was not uniformly distributed. Dissolution is localized along one or more discrete channels aligned with the general flow direction. Dissolution is maximum at the axes of the channels and then progressively decreases toward their margins. Development of dissolution channels reflects a positive-feedback process between flow rate, permeability, and dissolution rate. A high local fluid flux means a short residence time of the fluid in the fracture and a greater degree of undersaturation relative to quartz solubility compared to areas with a small fluid flux and the associated longer residence time of the fluid. A larger fluid flux is associated with a greater local permeability, which reflects the larger local hydraulic aperture.

The tendency to develop discrete fluid channels along a fracture in which dissolution occurs has important implications. The development of dissolution channel emphasizes the coupled nature of fluid flow and chemical processes. Furthermore, the formation of flow channels along a fracture invalidates application of the simple parallel-plate model to fluid flow in the fracture sustaining significant dissolution, because the parallel-plate model requires relatively uniform flow in the fracture.

Although the data are limited, there is a discernible relation between volumetric flow rate through the fracture and the rate of increase of permeability with time. All other factors being constant, the greater the volumetric flow rate, the greater the rate of permeability increase with time. This observation is consistent with the coupling between fluid residence time, flow rate and rate of dissolution noted above.

The permeability measured immediately before a temperature increase is always significantly bigger than the permeability measured immediately after establishing the

higher steady state temperature. The cause of this temperature dependence of the permeability is unknown.

The slow decrease of permeability observed in the initial interval of sustained flow could be related to either of two processes. The development of a small volume of secondary analcite occurs in the early stages of sustained flow and may decrease the fracture permeability as a consequence of reduction of the effective aperture of the fracture by blockage. Alternatively, the decrease of fracture permeability may reflect a slow rate of net closure of the fracture aperture as a consequence of pressure solution of the load-bearing asperities. These experiments are inadequate for the resolving between the two possibilities. The origin of the Al associated with formation of the analcite is uncertain; it may represent a contamination problem or it may be derived in part from the small amount of Al in quartz liberated during dissolution.

DISSOLUTION MODIFICATION OF AN ABRADED SURFACE

The systematic dissolution occurring transversely across a dissolution channel provides the opportunity to determine the evolution of the surface texture as a function of increasing dissolution. This is possible because the abrasion process generates a surface texture that is statistically homogeneous. Abrasion-induced microcracks in the surface of the abraded saw cut play the dominant role in controlling the dissolution modification of the surface texture with increasing dissolution, because the microcracks are the dominant loci for dissolution. Careful study of the SEM images across a transect of a major channel shows that five distinct dissolution-induced surface elements occur and exhibit systematic spatial variations in relation to the degree of dissolution. These distinctive dissolution elements originate from the initial surface microcracks and exhibit systematic morphology changes with increasing dissolution.

On the basis of the systematic spatial relations of these dissolution surface elements, two scenarios for the dissolution modification of a surface crack are inferred. The original dimensions of the microcrack, especially the depth of penetration, is the important factor determining which scenario a particular crack follows. Cracks that penetrate $< 10 \mu\text{m}$ follow one evolution scenario, whereas deeper cracks follow the other scenario. The stage to which a crack has evolved after a specific amount of dissolution is directly related to the original dimensions of the crack, particularly its depth of penetration. For the same net amount of dissolution, the shorter, shallower penetrating cracks attain more advanced stages in the evolution sequence than do the longer, deeper penetrating cracks. Thus, if

there is a distribution of crack dimensions in the surface, there is a corresponding distribution of dissolution surface elements at differing stages of the evolution scenarios.

The morphology of the dissolution elements derived from dissolution modification of cracks reflects in part the crystallographic control of dissolution of quartz. With increasing dissolution, walls of dissolution surface elements tend to acquire orientations parallel to specific crystallographic planes. For example, on the saw cut normal to the c-axis, the m-plane and the $\{11\bar{2}n\}$ (where n is 2 or 3) exert a significant crystallographic control on the morphology of dissolution surface elements at particular stages in their development. On the abraded m-plane (the end of the sample), the m-, r-, z- and s-planes exert a measurable crystallographic control on the morphology of dissolution surface elements.

Understanding the evolution of the overall surface texture with increasing dissolution is intimately tied to understanding the evolution of dissolution surface elements derived from cracks and their spatial relationship to their immediate neighbors. The overall surface is a composite of dissolution-induced surface elements derived from an initial population of surface cracks with a particular distribution of crack dimensions and spacings. As noted above, the distribution of the dimensions of the initial crack population influences the distribution of morphology and dimensions of dissolution surface elements occurring after a given amount of overall dissolution of the surface. In addition to the distribution of crack dimensions, the nature of spatial relations of neighboring cracks, such as distance to neighboring cracks or distance between cracks of particular dimensions, plays an important role in the evolution of the morphology of the overall surface.

With increasing dissolution, the areal extent of a dissolution surface element increases as a result of lateral retreat and/or laying back of the walls of the element. As the dissolution element enlarges areally it eventually impinges on its neighbors and vice versa. The relative depths of the neighboring dissolution elements determines the subsequent sequence of events. If the depths of the neighboring elements (i.e. the depths of the original cracks) differ significantly, then widening of the deeper element ultimately annihilates the shallower element. If depths of neighboring dissolution elements are similar, then there is a mutual annihilation of the elements. Clearly, the nature of "interference" of nearest neighbors strongly depends upon the distributional form of the initial surface microcrack populations. Populations with different frequency distributions of dimensions and spacings will give rise to different dissolution-induced surface textures, all other factors being constant.

REFERENCES CITED

- Ballman, A.A., and Landise, R.A., 1963, Hydrothermal growth of crystals: in Gilman, J., ed., *The Art and Science of Growing Crystals*: New York, John Wiley and Sons, chapter 13.
- Berner, R.A., 1978, *Rate control of mineral dissolution under earth surface conditions*: *American Journal of Science*, v. 278, p. 1235-1252.
- Correns, C.W., 1969, *Introduction to Mineralogy*: New York, Springer-Verlag.
- Fron del, C., 1962, *The system of mineralogy of James Dwight Dana and Edward Salisbury Dana*, Volume 3, 7th edition: New York, John Wiley and Sons.
- Gratz, A.J., Bird, P., and Quiro, G.B., 1990, Dissolution of quartz in aqueous basic solution, 106-236°C: Surface kinetics of perfect crystallographic faces: *Geochimica et Cosmochimica Acta*, v. 54, p. 2911-2922.
- Gross, R., 1918, *Zur Theorie des Wachstum- und Lösungsvorganges Kristalliner Materie*: *Abhandl. Math.-Natur. Kl. Sachs. Akad. Wiss.*, 35, 137
- Hicks, B.D., 1985, *Quartz Dissolution Features: An Experimental and Petrofabric Study* [M.S. thesis]: Columbia, Missouri, University of Missouri-Columbia.
- Hirth, J.P., and Pound, G.M., 1957, Evaporation of metal crystals: *Journal of Chemical Physics*, v. 26, p. 1216-1224.
- Johnson, B., 1983, *Modification of fracture surfaces by dissolution*: *Proc. 24th U.S. Symposium on Rock Mechanics*, p. 533-545.
- Joshi, M.S., and Vagh, A.S., 1968, *Application of the selective etch method in the study of structural defects in synthetic quartz*: *Soviet Physics-Crystallography*, v. 12, p. 573-580.

Liepmann, M.J., 1985, Chemical Durability of Crystalline and Vitreous Oxides in Alkaline Solution [Ph.D. dissert.]: Los Angeles, California, UCLA.

Wegner, M.W., and Christie, J.M., 1983, Chemical etching of deformation sub-structures in quartz: *Physics and Chemistry of Minerals*, v. 9, p. 67-78.

VITA

NAME: James Albert Bowman, Jr.

BIRTHDATE October 18, 1962

PARENTS: Mr. and Mrs. James Albert Bowman

PERMANENT ADDRESS: Post Office Box 169
Jeffersonville, Georgia 31044

EDUCATION: West Georgia College
Carrollton, Georgia
B.S., 1985, Geology

PROFESSIONAL EXPERIENCE:

1/89-12/90	K.W. Brown & Associates, Inc. College Station, Texas Project Manager/Hydrogeologist
2/91-12/91	Westinghouse Environmental and Geotechnical Services, Inc. Savannah, Georgia Hydrogeologist
2/92 - Present	South Carolina Department of Health and Environmental Control Columbia, South Carolina Hydrologist

PROFESSIONAL MEMBERSHIPS: Geologic Society of America
National Groundwater Association